

See discussions, stats, and author profiles for this publication at: <https://www.researchgate.net/publication/225977508>

Exterior Gravitation of a Polyhedron Derived and Compared with Harmonic and Mascon Gravitation Representations of Asteroid 4....

Article in *Celestial Mechanics and Dynamical Astronomy* · September 1996

DOI: 10.1007/BF00053511

CITATIONS

677

READS

1,540

2 authors, including:



[D. J. Scheeres](#)

University of Colorado Boulder

1,033 PUBLICATIONS 25,040 CITATIONS

[SEE PROFILE](#)

EXTERIOR GRAVITATION OF A POLYHEDRON DERIVED AND COMPARED WITH HARMONIC AND MASCON GRAVITATION REPRESENTATIONS OF ASTEROID 4769 CASTALIA

ROBERT A. WERNER and DANIEL J. SCHEERES

Jet Propulsion Laboratory, California Institute of Technology, Pasadena, California 91109, U.S.A.

(Received: 2 January 1996; accepted in final form: 1 August 1996)

Abstract. The exterior gravitation of a constant-density polyhedron is derived analytically in closed form. Expressions for potential, attraction, and gravity gradient matrix involve one logarithm term per edge and one arctangent term per face. The Laplacian can be used to determine whether a field point is inside or outside the polyhedron. This polyhedral method is well suited to evaluating the gravitational field of an irregularly shaped body such as an asteroid or comet. Conventional harmonic and mascon potential and attraction expressions suffer large errors when evaluated close to a polyhedral model of asteroid 4769 Castalia.

Key words: gravitational potential, polyhedron, mascon, asteroid 4769 Castalia.

1. Introduction

We wish to evaluate the gravitation of irregular-shaped bodies such as asteroids, comet nuclei, and small planetary satellites (we use the term ‘asteroid’ for all). Such bodies are not large enough for self-gravitation to shape them into spheres (Thomas *et al.*, 1986).

1.1. HARMONIC EXPANSION

The classical manner of representing arbitrary gravitational fields is by expanding the gravitational potential into a harmonic series and then explicitly computing the series coefficients (MacMillan, 1936; Kaula, 1966; Heiskanen *et al.*, 1967). Series coefficients are evaluated as integrals over the volume of the body, and for a constant density body may be reduced to integrals over the surface of the body (MacMillan, 1936). Alternately, the coefficients can be estimated from radio tracking data of spacecraft.

Such harmonic fields have many advantages: the series are guaranteed to converge to the correct gravity field outside of a circumscribing sphere; they can be truncated at finite order to size the accuracy in representation with the accuracy needed in modeling; and a rich literature exists for the computation and evaluation of such expansions.

However, harmonic expansions have several drawbacks. The first is that the harmonic expansion is always an approximation to a gravity field due to the finite truncation of the series expansion. The truncation error grows when evaluating

the gravity field close to the model's radius of convergence. Additional terms are necessary in the expansion to maintain a given accuracy.

The second major drawback is that the same form of the exterior harmonic expansion is no longer guaranteed to converge inside the circumscribing sphere, and indeed often diverges. (Convergence is shown to be an unstable property of a spherical harmonic series in Moritz (1980, Sections 6–8). A small change to the mass distribution might drive a convergent series to divergence, or *vice versa*.) Thus, the exterior harmonic expansion should not be used for studies of surface gravity or particle dynamics in that region. In planetary applications, the divergence may not exist or may be ignored, as the body will be nearly spherical. However, irregular body applications might require gravitation to be evaluated inside the circumscribing sphere where the divergence effects become quite strong. There are special procedures which may be applied for the computation of gravitational harmonics at the surface of an arbitrary body (Goździewski *et al.*, 1981; Grafarend *et al.*, 1994). However, they are generally cumbersome and are not valid in a global sense, but must be recomputed at each new radius of interest.

Another drawback is that the harmonic expansion yields no information about whether a field point is outside or inside the body. In a spacecraft simulation, a separate computer algorithm must be used to detect this important geometric condition (a spacecraft becomes kinetically challenged if it flies into an asteroid).

1.2. MASS CONCENTRATIONS

A second, commonly used approach for evaluating asteroid gravitation is to fill the body with point masses ('mascons' – mass concentrations) on an evenly spaced grid (Geissler *et al.*, 1995). The points are assigned individual masses so that the total asteroid mass is realized.

The mascon approach is simple to develop but has several deficiencies. First, like the harmonic approach, mascon gravitation provides no information about whether the field point is inside or outside the body. Second, for a given computational effort, the mascon approach is less accurate than a harmonic approach (in its region of convergence). Third, although the mascon approach does not diverge, and will converge onto the true gravity field in the limit as the number of individual mascons become arbitrarily large, there are significant errors in the force computation (even for large numbers of mascons) as will be shown.

1.3. POLYHEDRON

In this paper we investigate a third approach, which is to model the asteroid as a constant-density polyhedron. The polyhedron can have concavities in its surface (e.g. craters), overhangs, interior voids (caves), and even holes all the way through (torus). There is no special penalty for including small details, i.e. the entire body does not have to be modeled at a uniformly high resolution. As shown below, the

exterior gravitation of a constant-density polyhedron can be derived analytically and expressed in closed form.

The polyhedral approach remedies several drawbacks outlined above. First, the gravity field is exact for the given shape and density. Errors can be reduced entirely to errors in the asteroid shape determination and the level of discretization chosen for that shape. This is still, of course, an approximation to the true asteroid shape. However, since most asteroid shape determinations have a limited shape resolution, this approach provides gravitational accuracy consistent with the accuracy of the shape determination.

Second, polyhedron gravitation is a valid and exact solution up to the surface of the body. There is no region of divergence. This makes it attractive for evaluating the gravitational forces acting at the surface of the body, and in studying the dynamics of particles launched from the surface (Scheeres *et al.*, 1995).

Third, a polyhedron algorithm can detect whether a field point is outside or inside the polyhedron by evaluating the Laplacian of the gravitational potential. If the Laplacian vanishes (Laplace's equation), the field point is outside; otherwise inside (Poisson's equation). As will be seen, the Laplacian can be calculated with essentially no extra effort as the polyhedron potential or attraction are calculated.

Prior Work

Most papers on polyhedron gravitation appear in the geophysical literature, where polyhedra are used to represent buried ore bodies. Most evaluate polyhedron gravitation in closed form, although some accomplish only two analytic integrations and the third via numerical quadrature. Many derive only the attraction, or only the vertical component thereof.

Polyhedra can be classified in a taxonomy from simple to complex: (1) right rectangular parallelepiped (or 'brick'); (2) prism with polygonal cross-section; and (3) general polyhedron. The derivation of a brick's gravitation is not difficult: see, for instance, MacMillan (1930, section 43) or Waldvogel (1976). Modern geophysical interest in brick gravitation seems to have started with Nagy (1966) and extends through Bannerjee and Gupta (1977) and Montana *et al.* (1992). The gravitation of a prism is derived in Plouff (1976), Telford *et al.* (1976), and Cady (1980). In geophysical applications, vertical prisms usually extend to infinity downward, while horizontal prisms extend to infinity in both directions. We understand that polyhedron gravitation was first derived in the mid-1800s (Strakhov and Lapina 1990; Malovichko 1963), but we have not yet located the original works. Contemporary papers include Barnett (1976), Okabe (1979), Waldvogel (1979), Golizdra (1981), Pohánka (1988), Kwok (1991), Werner (1994), and Broucke (1995).

One way our polyhedron work differs from others' is that we pursue a geometric meaning for a certain subexpression, the solid angle subtended by a face when viewed from the field point. We have encountered only one other author who mentions this insight (MacMillan 1930, section 43), and that is for a special case. The insight leads to a subexpression requiring only one transcendental function

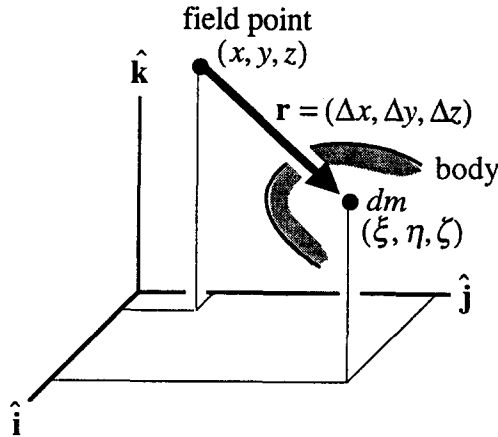


Figure 1. The field point is at Cartesian coordinates (x, y, z) and the differential mass dm at (ξ, η, ζ) . Vector \mathbf{r} extends from the field point to dm .

evaluation for each polyhedral face. Other papers require more than one, generally one transcendental per vertex of each face.

Another way our work differs is that our ultimate formulas are expressed intrinsically using vectors and distances. Other papers are cluttered with special coordinate systems and angles.

2. Derivation of Polyhedron Gravitation

By *polyhedron* we mean a three-dimensional solid body whose surface consists of planar faces meeting along straight edges or at isolated points called vertices. Exactly two faces meet at each edge. Three or more edges and a like number of faces meet at each vertex. Note: the vertex coordinates of a polyhedron alone are insufficient to describe it. The connective topology must also be described – edges connect which vertex pairs and bound which face pairs. Indeed, constructing a polyhedron by linking vertices is still an active research area (Hoppe *et al.*, 1992).

Our expressions admit a non-convex polyhedron with depressions in its surface, overhangs, interior voids, and holes all the way through. For asteroid gravitation, the two unrealistic assumptions we make are that (1) the asteroid is a polyhedron, and (2) the polyhedron's density is constant.

When necessary, we use a right-handed Cartesian coordinate system with basis vectors $\hat{\mathbf{i}}, \hat{\mathbf{j}}, \hat{\mathbf{k}}$ (unit vectors wear hats). Define vector $\mathbf{r} = \hat{\mathbf{i}}\Delta x + \hat{\mathbf{j}}\Delta y + \hat{\mathbf{k}}\Delta z$ from the unit mass at the field point (x, y, z) to the differential mass dm at (ξ, η, ζ) in the asteroid (Figure 1). Then $\Delta x = \xi - x; \Delta y = \eta - y; \Delta z = \zeta - z$; and $r^2 = \Delta x^2 + \Delta y^2 + \Delta z^2$; which means $d\Delta x = d\xi - dx$ etc. Also, $\nabla \mathbf{r} = (\hat{\mathbf{i}}\partial/\partial x + \hat{\mathbf{j}}\partial/\partial y + \hat{\mathbf{k}}\partial/\partial z)(\hat{\mathbf{i}}\Delta x + \hat{\mathbf{j}}\Delta y + \hat{\mathbf{k}}\Delta z) = -\mathbf{I}$.

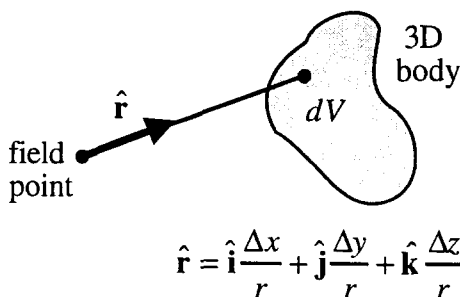


Figure 2. Vector $\hat{\mathbf{r}}$ is of unit length and points from the field point toward the differential element.

2.1. POTENTIAL

The divergence of vector field $\frac{1}{2}\hat{\mathbf{r}} = \mathbf{r}/2r$ with respect to the differential element's coordinates (ξ, η, ζ) is $1/r$. This identity allows us to convert the volume-integral definition of potential U to a surface integral via the Gauss divergence theorem, provided the density σ is constant:

$$\begin{aligned}
 U &\equiv G \iiint_M \frac{1}{r} dm = G\sigma \iiint_V \frac{1}{r} dV = \frac{1}{2}G\sigma \iiint_V \operatorname{div} \hat{\mathbf{r}} dV \\
 &= \frac{1}{2}G\sigma \iint_S \hat{\mathbf{n}} \cdot \hat{\mathbf{r}} dS,
 \end{aligned} \tag{1}$$

where G is the gravitational constant. Gauss expresses this result as a normal derivative $\frac{1}{2}G\sigma \iint_S (\partial r / \partial n) dS$ (MacMillan 1930, section 59). This general result holds for any constant-density 3D body that satisfies the preconditions of the divergence theorem, namely: the volume V must be bounded and connected, its surface S must be piecewise smooth and orientable, and the vector field and its first derivative must exist and be continuous throughout the volume and on its surface (Greenberg, 1978, Ch. 9).

Bodies such as spheres, ellipsoids, torii, bricks, and polyhedra satisfy these preconditions where the field point is outside. If the field point lies on or within the body, the vector field $\hat{\mathbf{r}}$ is undefined where the field point coincides with the differential element. We suspect the violation is benign and that the expressions below are correct in the interior.

2.1.1. Surface Integral for a Polyhedron's Potential

Now we specialize the 3D body to a polyhedron (Figure 3). Each face f of the polyhedron (i.e., a polygon) gets its own right-handed Cartesian coordinate system with the origin at the field point (to reduce clutter, we do not subscript basis vectors and coordinates). $\hat{\mathbf{k}}$ is aligned with $\hat{\mathbf{n}}_f$, the outward-pointing surface normal vector of face f . Specific directions of $\hat{\mathbf{i}}, \hat{\mathbf{j}}$ (paralleling the face plane) are unimportant.

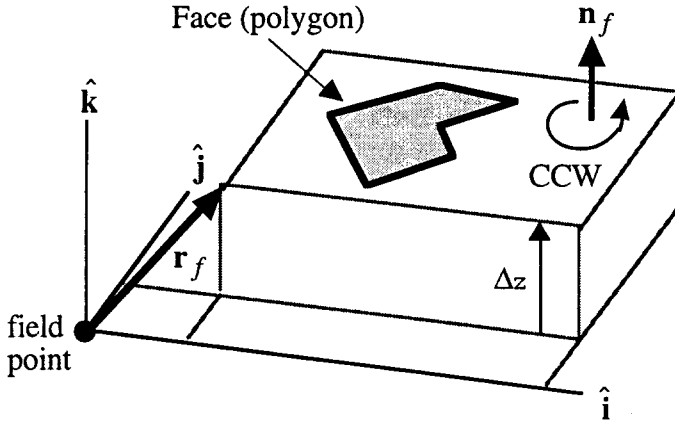


Figure 3. Each polyhedron face has its own Cartesian coordinate system oriented so that $\hat{\mathbf{k}}$ is aligned with the face's normal vector $\hat{\mathbf{n}}_f$. Vector \mathbf{r}_f extends from the field point to any point in the face plane. $\Delta z = \hat{\mathbf{n}}_f \cdot \mathbf{r}_f$ is the constant, signed, perpendicular distance from the field point to the face plane.

The components of \mathbf{r} , namely Δx , Δy , Δz , are expressed in this coordinate system, with Δz being constant.

To proceed, separate the surface integral (1) into a sum of integrals, one per face:

$$\begin{aligned}
 U &= \frac{1}{2} G \sigma \sum_{f \in \text{faces}} \iint_f \hat{\mathbf{n}}_f \cdot \hat{\mathbf{r}} \, dS = \frac{1}{2} G \sigma \sum_{f \in \text{faces}} \iint_f \hat{\mathbf{n}}_f \cdot \left(\frac{\mathbf{r}}{r} \right) \, dS \\
 &= \frac{1}{2} G \sigma \sum_{f \in \text{faces}} \hat{\mathbf{n}}_f \cdot \mathbf{r}_f \iint_f \frac{1}{r} \, dS.
 \end{aligned} \tag{2}$$

Since we integrate over a plane, the quantity $\Delta z = \hat{\mathbf{n}}_f \cdot \mathbf{r}$ is constant. In bringing that factor outside the integral, we replace $\mathbf{r} \rightarrow \mathbf{r}_f$, a vector from the field point to some fixed point in the face plane. Its sole use is to calculate Δz by dotting with $\hat{\mathbf{n}}_f$.

2.1.2. Potential of a Planar Region

We recognize the integral $\iint dS/r$ in Equation (2) as the potential of a 2D planar region. Although in (2) the region is a polygon, we can as easily derive a result for a general planar region S by performing an add-subtract trick and invoking Green's theorem. An integral $\iint (\Delta z/r^3) \, dS$ appears, which we label ω_f and deal with later:

$$\begin{aligned}
 \iint_S \frac{1}{r} \, dS &= \iint_S \left(\frac{1}{r} + \frac{\Delta z^2}{r^3} \right) \, dS - \iint_S \frac{\Delta z^2}{r^3} \, dS \\
 &= \iint_S \left(\frac{r^2 - \Delta x^2}{r^3} + \frac{r^2 - \Delta y^2}{r^3} \right) \, dS - \Delta z \iint_S \frac{\Delta z}{r^3} \, dS
 \end{aligned}$$

$$\begin{aligned}
&= \iint_S \left(\frac{\partial}{\partial \Delta x} \frac{\Delta x}{r} + \frac{\partial}{\partial \Delta y} \frac{\Delta y}{r} \right) dS - \Delta z \cdot \omega_f \\
&= \oint_C \frac{1}{r} (\Delta x d\Delta y - \Delta y d\Delta x) - \hat{\mathbf{n}}_f \cdot \mathbf{r}_f \cdot \omega_f
\end{aligned} \tag{3}$$

where C is the boundary of the region, traversed counterclockwise according to $\hat{\mathbf{n}}_f$ and the right-hand rule. A planar region's potential can be evaluated as a line integral around the boundary and another term involving the entire region.

2.1.3. ω_f Interpreted

In so many words, the integral

$$\omega_f \equiv \iint_S \frac{\Delta z}{r^3} dS \tag{4}$$

is the signed solid angle subtended by planar region S when viewed from the field point. Alternately, it is the signed area of S when projected onto a unit sphere centered on the field point.

As proof, let r be the distance from the field point O to the differential surface element dS in the plane (Figure 4). Let $\hat{\mathbf{n}}_f$ be the plane's normal vector, and let $\hat{\mathbf{r}}$ be the normal vector of the corresponding differential surface element $d\omega$ on the unit sphere. Due to the projection, area $d\omega$ is proportional to dS/r^2 , further modulated by the cosine of the angle between the two normal vectors $\hat{\mathbf{n}}_f$ and $\hat{\mathbf{r}}$:

$$d\omega = \frac{1}{r^2} \hat{\mathbf{r}} \cdot \hat{\mathbf{n}}_f dS = \frac{1}{r^2} \frac{\mathbf{r}}{r} \cdot \hat{\mathbf{n}}_f dS = \frac{\Delta z}{r^3} dS.$$

When we integrate over the entire planar region S , the result (4) follows. An alternate proof using differential geometry appears in Werner (1994, Appendix A).

Due to the projection (a plane onto a sphere), the magnitude of ω_f cannot exceed the area of one hemisphere, or 2π steradians.

Although the area of the planar region S is positive, ω_f is signed according to Δz (Figure 4). That is, when $\hat{\mathbf{r}}$ points in the same general direction as $\hat{\mathbf{n}}_f$, $\omega_f > 0$, and when $\hat{\mathbf{r}}$ generally opposes $\hat{\mathbf{n}}_f$, $\omega_f < 0$.

There is more to be said about ω_f ; in particular, how to evaluate it. We postpone this matter until after we finish the polyhedron gravitation derivations.

2.1.4. Potential of a Polygon

We had just derived the potential of a general 2D region (Equation 3). Next specialize the region to be a polygon, e.g. a face of a polyhedron. Integral (3) can be written as a sum over the polygon edges e :

$$\iint_{\text{polygon}} \frac{1}{r} dS = \sum_{e \in \text{edges}} \int_e \frac{1}{r} (\Delta x d\Delta y - \Delta y d\Delta x) - \hat{\mathbf{n}}_f \cdot \mathbf{r}_f \cdot \omega_f. \tag{5}$$

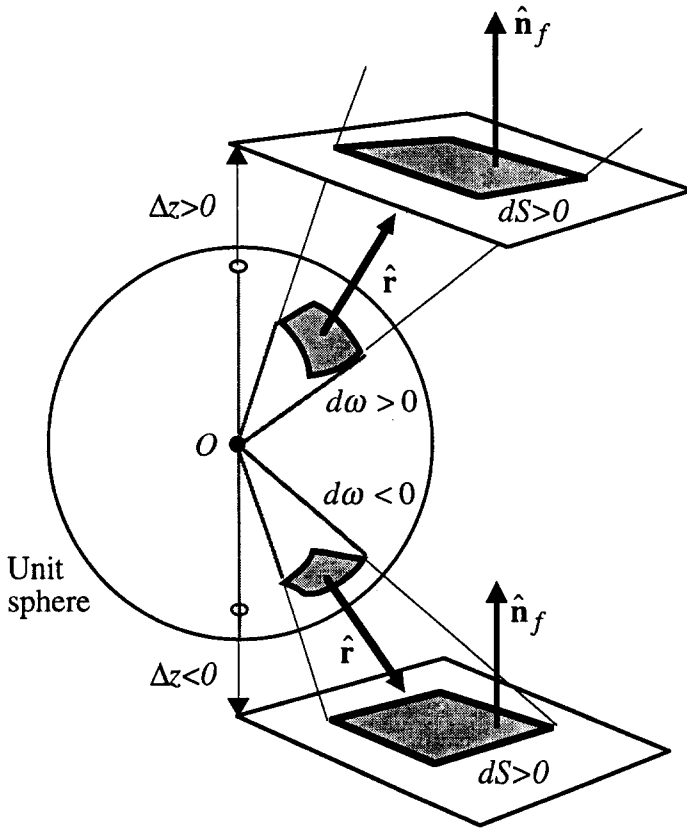


Figure 4. Planar area element dS is projected onto a unit sphere centered at the field point O . The resulting spherical area $d\omega$ has the same sign as Δz .

Next concentrate on a typical edge e (Figure 5). Each edge has an edge normal vector $\hat{\mathbf{n}}_e^f$ which lies in the face plane, is orthogonal to both the along-the-edge vector and the face normal vector, and points outward. Define angle α_e between the edge and the face's $\hat{\mathbf{i}}$ axis in terms of this edge-normal vector: $\cos \alpha_e = -\hat{\mathbf{n}}_e^f \cdot \hat{\mathbf{j}}$ and $\sin \alpha_e = +\hat{\mathbf{n}}_e^f \cdot \hat{\mathbf{i}}$.

With these definitions, we can evaluate the integral in (5) for typical polygon edge e . Let s parameterize the distance from some fixed point $(\Delta x_e, \Delta y_e)$ on the edge or its infinite extension. The 2D coordinates $(\Delta x, \Delta y)$ of a general point along the edge are $(\Delta x_e + s \cos \alpha_e, \Delta y_e + s \sin \alpha_e)$. Then

$$\begin{aligned} & \int_e \frac{1}{r} (\Delta x d\Delta y - \Delta y d\Delta x) \\ &= \int_e \frac{1}{r} \begin{bmatrix} (\Delta x_e + s \cos \alpha_e) \sin \alpha_e ds \\ -(\Delta y_e + s \sin \alpha_e) \cos \alpha_e ds \end{bmatrix} \end{aligned}$$

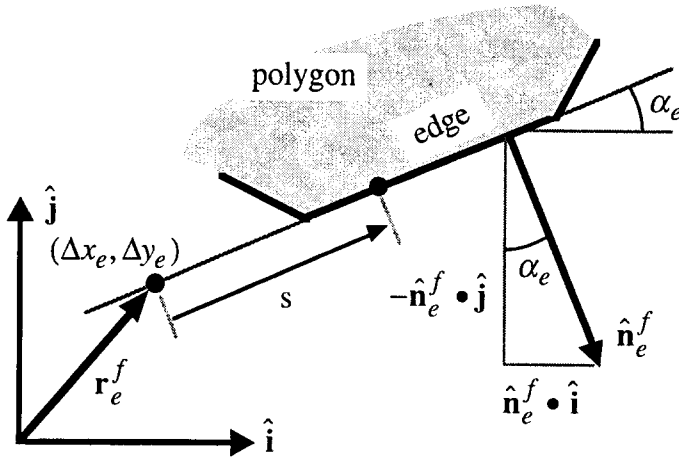


Figure 5. A typical edge e of polygon f is inclined by angle α_e relative to the polygon's $\hat{\mathbf{i}}$ axis. The edge-normal vector $\hat{\mathbf{n}}_e^f$ lies in the $\hat{\mathbf{i}} - \hat{\mathbf{j}}$ plane, is perpendicular to the edge, and points outward. Points on the edge are parametrized by distance s from a fixed point \mathbf{r}_e^f on the edge or its infinite extension.

$$\begin{aligned}
 &= (\Delta x_e \sin \alpha_e - \Delta y_e \cos \alpha_e) \int_e \frac{1}{r} ds = (\hat{\mathbf{n}}_e^f \cdot \hat{\mathbf{i}} \Delta x_e + \hat{\mathbf{n}}_e^f \cdot \hat{\mathbf{j}} \Delta y_e) \int_e \frac{1}{r} ds \\
 &= \hat{\mathbf{n}}_e^f \cdot \mathbf{r}_e^f \int_e \frac{1}{r} ds,
 \end{aligned} \tag{6}$$

where $\mathbf{r}_e^f \equiv \hat{\mathbf{i}} \Delta x_e + \hat{\mathbf{j}} \Delta y_e + \hat{\mathbf{k}} \Delta z_e$ is a vector from the field point to the fixed point on edge e of face f (later we will drop the superscript f). Since $\hat{\mathbf{n}}_e^f \cdot \hat{\mathbf{k}} = 0$, \mathbf{r}_e^f need not lie in the face plane.

2.1.5. Potential of a Wire

We recognize the integral $\int ds/r$ in Equation (6) as the potential of a 1D straight 'wire'. We adopt the symbol $L_e^f \equiv \int_e r^{-1} ds$ for the general edge e of face f (later we will drop the superscript f). MacMillan (1930, Sections 31 and 43) and Werner (1994) show the definite integral can be expressed intrinsically in terms of the distances a and b from the field point to the edge's two ends and the edge length e (Figure 6):

$$L_e^f = \int_e \frac{1}{r} ds = \ln \frac{a + b + e}{a + b - e}. \tag{7}$$

2.1.6. Backtracking to Polyhedron Potential

With (7), Equation (6) reads simply $\hat{\mathbf{n}}_e^f \cdot \mathbf{r}_e^f \cdot L_e^f$. In turn, the potential of a 2D polygon (Equation 5) is

$$\iint_{\text{polygon}} \frac{1}{r} dS = \sum_{e \in \text{polygon's edges}} \hat{\mathbf{n}}_e^f \cdot \mathbf{r}_e^f \cdot L_e^f - \hat{\mathbf{n}}_f \cdot \mathbf{r}_f \cdot \omega_f. \tag{8}$$

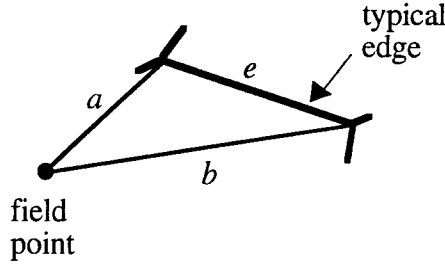


Figure 6. Constant edge-length e and variable distances a and b are needed to evaluate L_e^f .

When we substitute this polygon result into the polyhedron expression (2), we find:

$$\begin{aligned}
 U &= \frac{1}{2} G \sigma \sum_{f \in \text{faces}} \hat{\mathbf{n}}_f \cdot \mathbf{r}_f \iint_f \frac{1}{r} dS \\
 &= \frac{1}{2} G \sigma \sum_{f \in \text{faces}} \mathbf{r}_f \cdot \hat{\mathbf{n}}_f \left[\left(\sum_{e \in \text{face's edges}} \hat{\mathbf{n}}_e^f \cdot \mathbf{r}_e^f \cdot L_e^f \right) - \hat{\mathbf{n}}_f \cdot \mathbf{r}_f \cdot \omega_f \right] \\
 &= \frac{1}{2} G \sigma \sum_{f \in \text{faces}} \left(\sum_{e \in \text{face's edges}} \hat{\mathbf{r}}_f \cdot \hat{\mathbf{n}}_f \hat{\mathbf{n}}_e^f \cdot \mathbf{r}_e^f \cdot L_e^f \right) \\
 &\quad - \frac{1}{2} G \sigma \sum_{f \in \text{faces}} \hat{\mathbf{r}}_f \cdot \mathbf{n}_f \hat{\mathbf{n}}_f \cdot \mathbf{r}_f \cdot \omega_f.
 \end{aligned} \tag{9}$$

2.1.7. Common Edges

We can simplify the nested sums in Equation (9). First, substitute $\mathbf{r}_f \rightarrow \mathbf{r}_e^f$ because $\mathbf{r}_f \cdot \hat{\mathbf{n}}_f = \Delta z = \mathbf{r}_e^f \cdot \hat{\mathbf{n}}_f$ for all the various \mathbf{r}_e^f of a face's edges. Next concentrate on a typical edge, for example $\overline{P_1 P_2}$, in common with faces A and B (Figure 7). Exactly two terms of the nested sums are involved with this edge, one from face A and one from B . We can choose the same \mathbf{r}_e^f vector for both faces, i.e. $\mathbf{r}_{12}^A = \mathbf{r}_{21}^B = \mathbf{r}_{12}$. Also, the integrals $L_{12}^A = L_{21}^B = L_{12}$ for both A and B , since they depend only on the edge length and the distances from the field point to the two ends. The nested sums becomes a single summation over the polyhedron edges:

$$\begin{aligned}
 &\sum_{f \in \text{faces}} \left(\sum_{e \in \text{face's edges}} \mathbf{r}_e^f \cdot \hat{\mathbf{n}}_f \hat{\mathbf{n}}_e^f \cdot \mathbf{r}_e^f \cdot L_e^f \right) \\
 &= \left\{ \cdots + \mathbf{r}_{12}^A \cdot \hat{\mathbf{n}}_A \hat{\mathbf{n}}_{12}^A \cdot \mathbf{r}_{12}^A \cdot L_{12}^A + \cdots \right\} \\
 &\quad + \left\{ \cdots + \mathbf{r}_{21}^B \cdot \hat{\mathbf{n}}_B \hat{\mathbf{n}}_{21}^B \cdot \mathbf{r}_{21}^B \cdot L_{21}^B + \cdots \right\}
 \end{aligned}$$

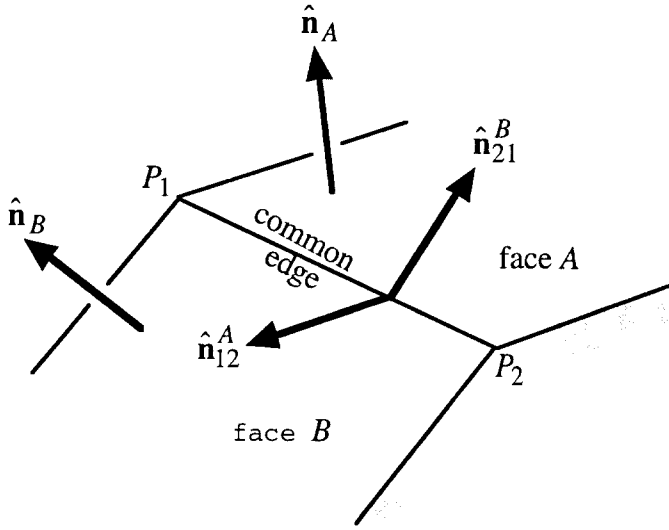


Figure 7. Two face-normal and edge-normal vectors are associated with each edge.

$$\begin{aligned}
 &= \{\cdots + \mathbf{r}_{12} \bullet (\hat{\mathbf{n}}_A \hat{\mathbf{n}}_{12}^A + \hat{\mathbf{n}}_B \hat{\mathbf{n}}_{21}^B) \bullet \mathbf{r}_{12} \cdot L_{12} + \cdots\} \\
 &= \{\cdots + \mathbf{r}_{12} \bullet \mathbf{E}_{12} \bullet \mathbf{r}_{12} \cdot L_{12} + \cdots\} \\
 &= \sum_{e \in \text{edges}} \mathbf{r}_e \bullet \mathbf{E}_e \bullet \mathbf{r}_e \cdot L_e.
 \end{aligned}$$

Here, \mathbf{r}_e is a vector from the field point to any point on edge e or its infinite extension. As promised, we have dispensed with the superscript f .

2.1.8. Dyads

We have defined a dyad $\mathbf{E}_{12} \equiv \hat{\mathbf{n}}_A \hat{\mathbf{n}}_{12}^A + \hat{\mathbf{n}}_B \hat{\mathbf{n}}_{21}^B$ in terms of the two face- and edge-normal vectors associated with edge $\overline{P_1 P_2}$; each edge has its own such \mathbf{E}_e . In looking back to Equation (9), it is also convenient to define another dyad $\mathbf{F}_f \equiv \hat{\mathbf{n}}_f \hat{\mathbf{n}}_f$, one for each face.

One conventionally uses matrices instead of dyads. We use them here because results are expressed intrinsically; not in any particular coordinate system. Dyads are described in Goldstein (1980, pp. 192–195) and Greenwood (1988, pp. 315–318). In matrix notation, dyad \mathbf{E}_{12} is expressed as $\hat{\mathbf{n}}_A (\hat{\mathbf{n}}_{12}^A)^T + \hat{\mathbf{n}}_B (\hat{\mathbf{n}}_{21}^B)^T$, the sum of two outer products; a 3×3 matrix. \mathbf{F}_f is simply the outer product of vector $\hat{\mathbf{n}}_f$ with itself.

\mathbf{F}_f is symmetric by construction. To show \mathbf{E}_e is likewise symmetric, evaluate it in a special Cartesian coordinate system $\hat{\mathbf{I}}, \hat{\mathbf{J}}, \hat{\mathbf{K}}$ (Figure 8). Align the $\hat{\mathbf{K}}$ vector parallel to \mathbf{E} 's edge (along the figure's lines-of-sight) and the $\hat{\mathbf{I}}$ vector to bisect the dihedral angle θ between faces A and B . Our convention is that $\hat{\mathbf{I}}$ points inward, although this is not crucial.

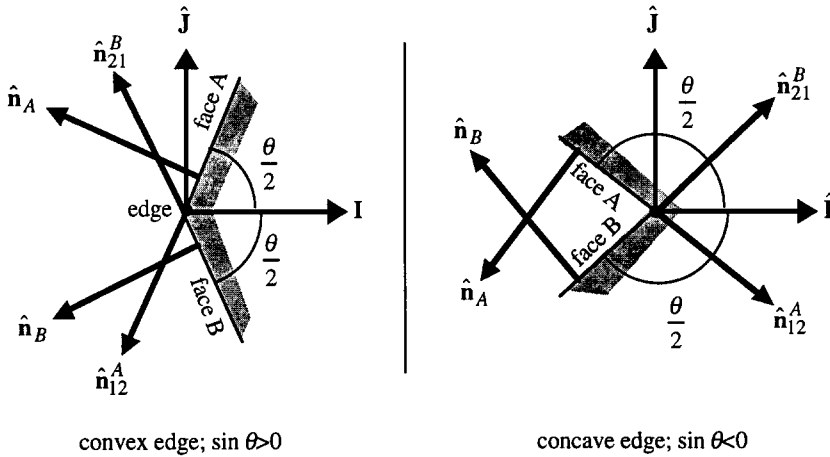


Figure 8. In a special $\hat{\mathbf{I}}, \hat{\mathbf{J}}, \hat{\mathbf{K}}$ coordinate system, the matrix corresponding to the edge dyad \mathbf{E}_e is diagonal, with $+\sin \theta$, $-\sin \theta$, and 0 on the diagonal. θ is the dihedral angle of the two faces.

The face and edge normal vectors lie in the $\hat{\mathbf{I}}, \hat{\mathbf{J}}$ plane. The face normal vectors are

$$\hat{\mathbf{n}}_A = \cos\left(\frac{\theta}{2} + 90^\circ\right) \hat{\mathbf{I}} + \sin\left(\frac{\theta}{2} + 90^\circ\right) \hat{\mathbf{J}} = -\sin\frac{\theta}{2} \hat{\mathbf{I}} + \cos\frac{\theta}{2} \hat{\mathbf{J}}$$

$$\hat{\mathbf{n}}_B = \cos\left(-\frac{\theta}{2} - 90^\circ\right) \hat{\mathbf{I}} + \sin\left(-\frac{\theta}{2} - 90^\circ\right) \hat{\mathbf{J}} = -\sin\frac{\theta}{2} \hat{\mathbf{I}} - \cos\frac{\theta}{2} \hat{\mathbf{J}}$$

and the edge normal vectors are

$$\hat{\mathbf{n}}_{12}^A = \cos\left(\frac{\theta}{2} + 180^\circ\right) \hat{\mathbf{I}} + \sin\left(\frac{\theta}{2} + 180^\circ\right) \hat{\mathbf{J}} = -\cos\frac{\theta}{2} \hat{\mathbf{I}} - \sin\frac{\theta}{2} \hat{\mathbf{J}}$$

$$\hat{\mathbf{n}}_{21}^B = \cos\left(-\frac{\theta}{2} - 180^\circ\right) \hat{\mathbf{I}} + \sin\left(-\frac{\theta}{2} - 180^\circ\right) \hat{\mathbf{J}} = -\cos\frac{\theta}{2} \hat{\mathbf{I}} + \sin\frac{\theta}{2} \hat{\mathbf{J}}$$

Then

$$\begin{aligned} \mathbf{E}_{12} &= \hat{\mathbf{n}}_A \hat{\mathbf{n}}_{12}^A + \hat{\mathbf{n}}_B \hat{\mathbf{n}}_{21}^B \\ &= \left[\begin{aligned} &\left(-\sin\frac{\theta}{2} \hat{\mathbf{I}} + \cos\frac{\theta}{2} \hat{\mathbf{J}}\right) \left(-\cos\frac{\theta}{2} \hat{\mathbf{I}} - \sin\frac{\theta}{2} \hat{\mathbf{J}}\right) \\ &+ \left(-\sin\frac{\theta}{2} \hat{\mathbf{I}} - \cos\frac{\theta}{2} \hat{\mathbf{J}}\right) \left(-\cos\frac{\theta}{2} \hat{\mathbf{I}} + \sin\frac{\theta}{2} \hat{\mathbf{J}}\right) \end{aligned} \right] \\ &= \left[\begin{aligned} &\sin\frac{\theta}{2} \cos\frac{\theta}{2} \hat{\mathbf{I}}\hat{\mathbf{I}} - \cos^2\frac{\theta}{2} \hat{\mathbf{J}}\hat{\mathbf{I}} + \sin^2\frac{\theta}{2} \hat{\mathbf{I}}\hat{\mathbf{J}} - \sin\frac{\theta}{2} \cos\frac{\theta}{2} \hat{\mathbf{J}}\hat{\mathbf{J}} \\ &+ \sin\frac{\theta}{2} \cos\frac{\theta}{2} \hat{\mathbf{I}}\hat{\mathbf{I}} + \cos^2\frac{\theta}{2} \hat{\mathbf{J}}\hat{\mathbf{I}} - \sin^2\frac{\theta}{2} \hat{\mathbf{I}}\hat{\mathbf{J}} - \sin\frac{\theta}{2} \cos\frac{\theta}{2} \hat{\mathbf{J}}\hat{\mathbf{J}} \end{aligned} \right] \end{aligned}$$

$$= \left[2 \sin \frac{\theta}{2} \cos \frac{\theta}{2} \hat{\mathbf{I}}\hat{\mathbf{I}} - 2 \sin \frac{\theta}{2} \cos \frac{\theta}{2} \hat{\mathbf{J}}\hat{\mathbf{J}} \right] = \sin \theta [\hat{\mathbf{I}}\hat{\mathbf{I}} - \hat{\mathbf{J}}\hat{\mathbf{J}}]$$

which shows that \mathbf{E} is symmetric in all coordinate systems. When rendered as a 3×3 matrix in this coordinate system, \mathbf{E} is a diagonal matrix with $+\sin \theta$, $-\sin \theta$, and zero on the diagonal.

2.1.9. Conclusion: Potential of a Polyhedron

After we incorporate all substitutions and definitions into Equation (9), the potential of a constant-density polyhedron is expressed as

$$U = \frac{1}{2} G \sigma \sum_{e \in \text{edges}} \mathbf{r}_e \bullet \mathbf{E}_e \bullet \mathbf{r}_e \cdot L_e - \frac{1}{2} G \sigma \sum_{f \in \text{faces}} \mathbf{r}_f \bullet \mathbf{F}_f \bullet \mathbf{r}_f \cdot \omega_f. \quad (10)$$

2.2. ATTRACTION

Before differentiating Equation (10) to derive 3D polyhedron attraction, we first derive the attraction of a 2D polygon in two different ways. Extra terms appear in the second which must cancel because they are absent from the first. The terms which cancel in 2D expressions markedly simplify 3D expressions.

First, differentiate the integral definition of a general planar region's potential, again using Green's theorem:

$$\begin{aligned} \nabla \iint_S \frac{1}{r} dS &= \left(\hat{\mathbf{i}} \frac{\partial}{\partial x} + \hat{\mathbf{j}} \frac{\partial}{\partial y} + \hat{\mathbf{k}} \frac{\partial}{\partial z} \right) \iint_S \frac{1}{r} dS \\ &= -\hat{\mathbf{i}} \iint_S \frac{\partial}{\partial \Delta x} \frac{1}{r} dS - \hat{\mathbf{j}} \iint_S \frac{\partial}{\partial \Delta y} \frac{1}{r} dS - \hat{\mathbf{k}} \iint_S \frac{\partial}{\partial \Delta z} \frac{1}{r} dS \\ &= -\hat{\mathbf{i}} \iint_S \left[\frac{\partial}{\partial \Delta x} \left(\frac{1}{r} \right) + \frac{\partial}{\partial \Delta y} (0) \right] dS \\ &\quad - \hat{\mathbf{j}} \iint_S \left[\frac{\partial}{\partial \Delta x} (0) + \frac{\partial}{\partial \Delta y} \left(\frac{1}{r} \right) \right] dS + \hat{\mathbf{k}} \iint_S \frac{\Delta z}{r^3} dS \\ &= -\hat{\mathbf{i}} \oint_C \frac{1}{r} d\Delta y + \hat{\mathbf{j}} \oint_C \frac{1}{r} d\Delta x + \hat{\mathbf{k}} \omega_f. \end{aligned}$$

Now restrict the planar region to be a polygon. The boundary integrals become a sum of line integrals along the straight edges:

$$\nabla \iint_{\text{polygon}} \frac{1}{r} dS = \sum_{e \in \text{edges}} \left[-\hat{\mathbf{i}} \int_e \frac{1}{r} d\Delta y + \hat{\mathbf{j}} \int_e \frac{1}{r} d\Delta x \right] + \hat{\mathbf{k}} \omega_f$$

$$\begin{aligned}
&= \sum_{e \in \text{edges}} \left[-\hat{\mathbf{i}} \sin \alpha_e \int_e \frac{1}{r} ds + \hat{\mathbf{j}} \cos \alpha_e \int_e \frac{1}{r} ds \right] + \hat{\mathbf{k}} \omega_f \\
&= \sum_{e \in \text{edges}} [-\hat{\mathbf{i}}(\hat{\mathbf{i}} \cdot \hat{\mathbf{n}}_e^f) \cdot L_e^f - \hat{\mathbf{j}}(\hat{\mathbf{j}} \cdot \hat{\mathbf{n}}_e^f) \cdot L_e^f] + \hat{\mathbf{n}}_f \omega_f \\
&= - \sum_{e \in \text{edges}} \hat{\mathbf{n}}_e^f L_e^f + \hat{\mathbf{n}}_f \omega_f. \tag{11}
\end{aligned}$$

Again, $\hat{\mathbf{k}} \cdot \hat{\mathbf{n}}_e^f = 0$. This concise formula expresses the attraction of a 2D polygon.

2.2.1. Canceling Terms

To reveal the terms which cancel one another, rederive the 2D polygon attraction by differentiating the polygon potential result (8). Recall that $\nabla \mathbf{r} = -\mathbf{I}$:

$$\begin{aligned}
&\nabla \left(\sum_{e \in \text{edges}} \hat{\mathbf{n}}_e^f \cdot \mathbf{r}_e^f \cdot L_e^f - \hat{\mathbf{n}}_f \cdot \mathbf{r}_f \cdot \omega_f \right) \\
&= \sum_{e \in \text{edges}} (\hat{\mathbf{n}}_e^f \cdot \nabla \mathbf{r}_e^f \cdot L_e^f + \hat{\mathbf{n}}_e^f \cdot \mathbf{r}_e^f \cdot \nabla L_e^f) - \hat{\mathbf{n}}_f \cdot \nabla \mathbf{r}_f \cdot \omega_f - \hat{\mathbf{n}}_f \cdot \mathbf{r}_f \cdot \nabla \omega_f \\
&= \left[- \sum_{e \in \text{edges}} \hat{\mathbf{n}}_e^f \cdot L_e^f + \hat{\mathbf{n}}_f \cdot \omega_f \right] + \left\{ \sum_{e \in \text{edges}} \hat{\mathbf{n}}_e^f \cdot \mathbf{r}_e^f \cdot \nabla L_e^f - \hat{\mathbf{n}}_f \cdot \mathbf{r}_f \cdot \nabla \omega_f \right\}.
\end{aligned}$$

The first two terms (in brackets) are Equation (11). Thus the last two terms (in braces) cancel. We write them thus:

$$\sum_{e \in \text{edges}} \hat{\mathbf{n}}_e^f \cdot \mathbf{r}_e^f \cdot \nabla L_e^f = \hat{\mathbf{n}}_f \cdot \mathbf{r}_f \cdot \nabla \omega_f. \tag{12}$$

MacMillan (1930, Section 45) notes that such canceling terms occur with any homogeneous (constant-density) body.

To prepare for the 3D case, multiply (12) through by $\mathbf{r}_f \cdot \hat{\mathbf{n}}_f$, sum over all polyhedral faces, expand the nested sums as before, and collect the common edge terms. The result is

$$\sum_{e \in \text{edges}} \mathbf{r}_e \cdot \mathbf{E}_e \cdot \mathbf{r}_e \cdot \nabla L_e = \sum_{f \in \text{faces}} \mathbf{r}_f \cdot \mathbf{F}_f \cdot \mathbf{r}_f \cdot \nabla \omega_f. \tag{13}$$

Also, multiply (12) through by only the face normal vector $\hat{\mathbf{n}}_f$ and follow the rest of the procedure to find

$$\sum_{e \in \text{edges}} \mathbf{E}_e \cdot \mathbf{r}_e \cdot \nabla L_e = \sum_{f \in \text{faces}} \mathbf{F}_f \cdot \mathbf{r}_f \cdot \nabla \omega_f. \tag{14}$$

2.2.2. Conclusion: Polyhedron Attraction

To find the attraction of a 3D polyhedron, formally differentiate the potential result (10):

$$\begin{aligned}
 \nabla U &= \frac{1}{2}G\sigma \nabla \sum_{e \in \text{edges}} \mathbf{r}_e \bullet \mathbf{E}_e \bullet \mathbf{r}_e \cdot L_e - \frac{1}{2}G\sigma \nabla \sum_{f \in \text{faces}} \mathbf{r}_f \bullet \mathbf{F}_f \bullet \mathbf{r}_f \cdot \omega_f \\
 &= -G\sigma \left[\sum_{e \in \text{edges}} \mathbf{E}_e \bullet \mathbf{r}_e \cdot L_e - \sum_{f \in \text{faces}} \mathbf{F}_f \bullet \mathbf{r}_f \cdot \omega_f \right] + \\
 &\quad + \frac{1}{2}G\sigma \left\{ \sum_{e \in \text{edges}} \mathbf{r}_e \bullet \mathbf{E}_e \bullet \mathbf{r}_e \cdot \nabla L_e - \sum_{f \in \text{faces}} \mathbf{r}_f \bullet \mathbf{F}_f \bullet \mathbf{r}_f \cdot \nabla \omega_f \right\}.
 \end{aligned}$$

The terms in braces cancel due to Equation (13) and Equation (15) remains:

$$\nabla U = -G\sigma \sum_{e \in \text{edges}} \mathbf{E}_e \bullet \mathbf{r}_e \cdot L_e + G\sigma \sum_{f \in \text{faces}} \mathbf{F}_f \bullet \mathbf{r}_f \cdot \omega_f. \quad (15)$$

2.3. GRAVITY GRADIENT MATRIX

To calculate the symmetric gravity gradient matrix of second partial derivatives, formally differentiate the attraction expression (15):

$$\begin{aligned}
 \nabla(\nabla U) &= -G\sigma \left(\nabla \sum_{e \in \text{edges}} \mathbf{E}_e \bullet \mathbf{r}_e \cdot L_e \right) + G\sigma \left(\nabla \sum_{f \in \text{faces}} \mathbf{F}_f \bullet \mathbf{r}_f \cdot \omega_f \right) \\
 &= G\sigma \left[\sum_{e \in \text{edges}} \mathbf{E}_e \cdot L_e - \sum_{f \in \text{faces}} \mathbf{F}_f \cdot \omega_f \right] + \\
 &\quad + G\sigma \left\{ \sum_{e \in \text{edges}} \mathbf{E}_e \bullet \mathbf{r}_e \cdot \nabla L_e - \sum_{f \in \text{faces}} \mathbf{F}_f \bullet \mathbf{r}_f \cdot \nabla \omega_f \right\}.
 \end{aligned}$$

The terms in braces cancel due to Equation (14) and (16) remains:

$$\nabla \nabla U = G\sigma \sum_{e \in \text{edges}} \mathbf{E}_e \cdot L_e - G\sigma \sum_{f \in \text{faces}} \mathbf{F}_f \cdot \omega_f. \quad (16)$$

2.4. LAPLACIAN OF A POLYHEDRON'S POTENTIAL

Although the Laplacian $\nabla^2 U$ can be calculated as the trace of the gravity gradient matrix (16), a formal differentiation of Equation (2) leads to a very simple result:

$$\begin{aligned}
 \nabla^2 U &= \frac{1}{2} G \sigma \left(\sum_{f \in \text{faces}} \nabla^2 \iint_f \hat{\mathbf{n}}_f \cdot \hat{\mathbf{r}} \, dS \right) \\
 &= \frac{1}{2} G \sigma \left(\sum_{f \in \text{faces}} \nabla^2 \iint_f \hat{\mathbf{k}} \cdot \left[\hat{\mathbf{i}} \frac{\Delta x}{r} + \hat{\mathbf{j}} \frac{\Delta y}{r} + \hat{\mathbf{k}} \frac{\Delta z}{r} \right] dS \right) \\
 &= \frac{1}{2} G \sigma \left(\sum_{f \in \text{faces}} \iint_f \nabla^2 \frac{\Delta z}{r} \, dS \right) = G \sigma \left(\sum_{f \in \text{faces}} \iint_f \frac{-\Delta z}{r^3} \, dS \right) \\
 &= -G \sigma \sum_{f \in \text{faces}} \omega_f. \tag{17}
 \end{aligned}$$

The sum $-\sum \omega_f$ vanishes where the field point is outside the polyhedron (Laplace's equation), and equals -4π inside (Poisson's equation).

The Laplacian can be calculated at essentially no cost as any of the potential, attraction, or gravity gradient matrix are calculated, since all require ω_f . A computer-based simulation can use the Laplacian to determine whether a field point is outside or inside what might be a complicated, gnarly polyhedron.

This concludes the gravitation derivation.

2.5. SOLID ANGLE

Two dimensionless scalars, L_e and ω_f , appear in the polyhedron gravitation expressions. A logarithm expression L_e is associated with each edge and a solid angle $\omega_f = \iint (\Delta z/r^3) \, dS$ is associated with each face. Equation (7) indicates how to calculate L_e . Here we show how to calculate ω_f for the simplest case, a triangle. Our approach is to use the alternate, spherical polygon interpretation, calculate its magnitude $|\omega_f| = \iint (|\Delta z|/r^3) \, dS$ using spherical geometry and vector algebra, then multiply by sign (Δz).

2.5.1. A Spherical Polygon's Area $|\omega_f|$

When the planar region S is a polygon (i.e. a face of a polyhedron), the image projected on the unit sphere centered on the field point is a spherical polygon whose edges are great-circular arcs (Figure 9). The (non-negative) area $|\omega_f|$ of a spherical polygon on a radius R sphere is $R^2 \left[\sum_{j=1}^n S_j - (n-2)\pi \right]$, where n is the number of vertices and S_j are the measures of the spherical vertex angles (CRC *Standard*

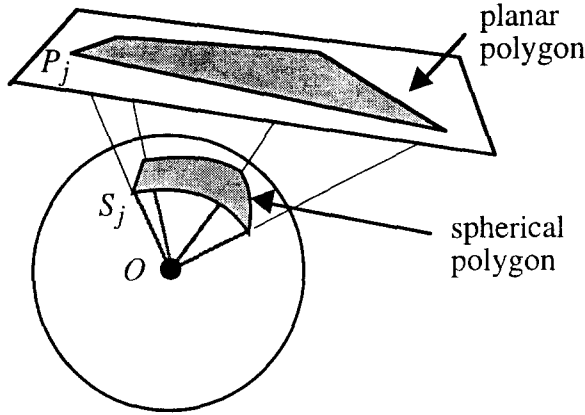


Figure 9. A planar polygon projected onto a sphere becomes a spherical polygon whose edges are great-circular arcs. The spherical polygon's area can be calculated from the spherical vertex angles S_j .

Mathematical Tables 1965, 'Mensuration Formulae'). The bracketed quantity is called the spherical excess; the sum of a spherical polygon's vertex angles $\sum S_j$ exceeds the sum of a corresponding planar polygon's $\sum P_j = (n - 2)\pi$. Since we use a unit sphere, $R = 1$ and we write simply

$$|\omega_f| = \sum_{j=1}^n S_j - (n - 2)\pi. \quad (18)$$

By knowing this formula for the area of a spherical polygon, we need not devise a way to integrate $\iint (|\Delta z|/r^3) dS$. Instead, we need to calculate the spherical vertex angles S_j .

2.5.2. A Spherical Polygon's Vertex Angles S_j

Here we develop vector expressions to calculate the sine and cosine of a spherical polygon's vertex angles S_j . Let $\mathbf{r}_i, \mathbf{r}_j, \mathbf{r}_k$ be vectors from the sphere's center O to three consecutive vertices P_i, P_j, P_k of the planar polygon (Figure 10). We use these to calculate two new vectors \mathbf{s}_{ji} and \mathbf{s}_{jk} which lie in planes $P_i - O - P_j$ and $P_j - O - P_k$ and which are tangent to the sphere, i.e. orthogonal to \mathbf{r}_j . After normalization, the dot and cross products of the two vectors yield the cosine and sine of S_j , the spherical vertex angle corresponding to P_j . For brevity we use c_{ij}, c_{jk} , and c_{ki} to represent the cosines of angles $P_i - O - P_j, P_j - O - P_k$, and $P_k - O - P_i$.

$$\mathbf{s}_{ji} \equiv (\mathbf{r}_j \times \mathbf{r}_i) \times \mathbf{r}_j = \mathbf{r}_i(\mathbf{r}_j \cdot \mathbf{r}_j) - \mathbf{r}_j(\mathbf{r}_i \cdot \mathbf{r}_j) = \mathbf{r}_i r_j^2 - \mathbf{r}_j(\mathbf{r}_i \cdot \mathbf{r}_j) = (\hat{\mathbf{r}}_i - \hat{\mathbf{r}}_j c_{ij}) r_i r_j^2,$$

$$\mathbf{s}_{jk} \equiv (\mathbf{r}_j \times \mathbf{r}_k) \times \mathbf{r}_j = \cdots = (\hat{\mathbf{r}}_k - \hat{\mathbf{r}}_j c_{jk}) r_k r_j^2.$$

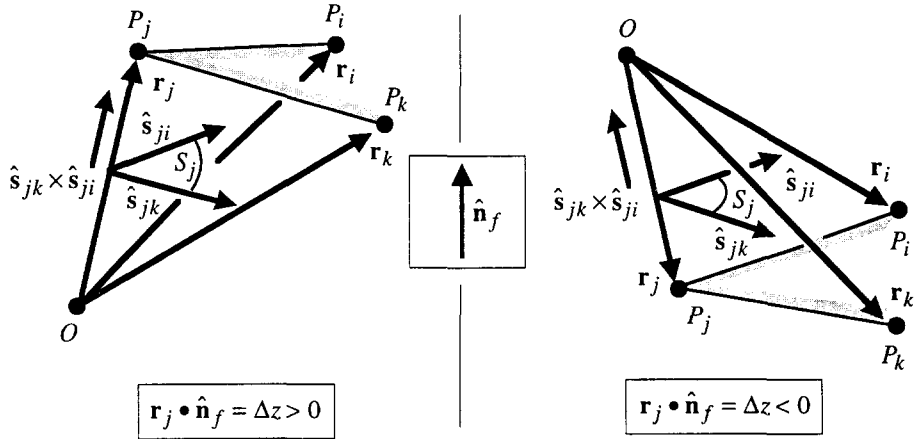


Figure 10. Given three consecutive planar vertices P_i, P_j, P_k , the sine and cosine of the spherical vertex angle S_j can be calculated by constructing vectors s_{ji} and s_{jk} .

The norms are

$$\begin{aligned} \|s_{ji}\|^2 &= s_{ji} \cdot s_{ji} = (\hat{\mathbf{r}}_i - \hat{\mathbf{r}}_j c_{ij}) \cdot (\hat{\mathbf{r}}_i - \hat{\mathbf{r}}_j c_{ij}) r_i^2 r_j^4 \\ &= [(\hat{\mathbf{r}}_i \cdot \hat{\mathbf{r}}_i) - 2(\hat{\mathbf{r}}_i \cdot \hat{\mathbf{r}}_j) c_{ij} + (\hat{\mathbf{r}}_j \cdot \hat{\mathbf{r}}_j) c_{ij}^2] r_i^2 r_j^4 = (1 - c_{ij}^2) r_i^2 r_j^4 \\ \|s_{jk}\|^2 &= s_{jk} \cdot s_{jk} = \dots = (1 - c_{jk}^2) r_k^2 r_j^4. \end{aligned}$$

Then the cosine of the spherical vertex angle S_j is

$$\begin{aligned} \cos S_j &= \hat{s}_{ji} \cdot \hat{s}_{jk} = \frac{(\hat{\mathbf{r}}_i - \hat{\mathbf{r}}_j c_{ij}) \cdot (\hat{\mathbf{r}}_k - \hat{\mathbf{r}}_j c_{jk})}{\sqrt{1 - c_{ij}^2} \sqrt{1 - c_{jk}^2}} \\ &= \frac{(\hat{\mathbf{r}}_i \cdot \hat{\mathbf{r}}_k) - (\hat{\mathbf{r}}_j \cdot \hat{\mathbf{r}}_k) c_{ij} - (\hat{\mathbf{r}}_i \cdot \hat{\mathbf{r}}_j) c_{jk} + (\hat{\mathbf{r}}_j \cdot \hat{\mathbf{r}}_j) c_{ij} c_{jk}}{\sqrt{1 - c_{ij}^2} \sqrt{1 - c_{jk}^2}} \\ &= \frac{c_{ik} - c_{ij} c_{jk}}{\sqrt{1 - c_{ij}^2} \sqrt{1 - c_{jk}^2}} \end{aligned} \quad (19)$$

which, in its way, expresses the law of cosines for spherical triangles.

A cross product yields a vector parallel to \mathbf{r}_j of length $\sin S_j$ (in Figure 10 it appears as a short vector paralleling \mathbf{r}_j). If we assume the polygon is convex (i.e. no vertex angle exceeds π radians), then each $\sin S_j > 0$. To calculate this magnitude, dot with $\hat{\mathbf{r}}_j$ and take the absolute value:

$$\sin S_j = |\hat{\mathbf{r}}_j \cdot (\hat{s}_{jk} \times \hat{s}_{ji})| = \frac{|\hat{\mathbf{r}}_j \cdot [(\hat{\mathbf{r}}_k - \hat{\mathbf{r}}_j c_{jk}) \times (\hat{\mathbf{r}}_i - \hat{\mathbf{r}}_j c_{ij})]|}{\sqrt{1 - c_{jk}^2} \sqrt{1 - c_{ij}^2}}$$

$$\begin{aligned}
&= \frac{|\hat{\mathbf{r}}_j \bullet [(\hat{\mathbf{r}}_k \times \hat{\mathbf{r}}_i) - (\hat{\mathbf{r}}_j \times \hat{\mathbf{r}}_i)c_{jk} - (\hat{\mathbf{r}}_k \times \hat{\mathbf{r}}_j)c_{ij}]|}{\sqrt{1 - c_{jk}^2} \sqrt{1 - c_{ij}^2}} \\
&= \frac{|\hat{\mathbf{r}}_i \bullet \hat{\mathbf{r}}_j \times \hat{\mathbf{r}}_k|}{\sqrt{1 - c_{jk}^2} \sqrt{1 - c_{ij}^2}}. \tag{20}
\end{aligned}$$

2.5.3. Calculating $|\omega_f|$ and ω_f

Having calculated a convex polygon's $\cos S_j$ and $\sin S_j$, we could calculate each S_j with arctangent and sum to calculate $|\omega_f| = [S_1 + S_2 + \dots + S_n - (n - 2)\pi] = [\arctan(\dots) + \arctan(\dots) + \dots - (n - 2)\pi]$. This approach requires n arctangent evaluations per polygon. However, another approach considers $|\omega_f|$ to be a sequence of plane rotations, first by S_1 , then by S_2 , etc. Use the various $\cos S_j$ and $\sin S_j$ in rotation matrices to calculate $\cos|\omega_f|$ and $\sin|\omega_f|$, from which a single arctangent yields $|\omega_f|$. To do this, regroup terms to read $|\omega_f| = \dots + (S_2 - \pi) + (S_1 - \pi) + (2\pi)$ and write down rotation matrices:

$$\begin{aligned}
&\begin{bmatrix} \cos|\omega_f| \\ \sin|\omega_f| \end{bmatrix} \\
&= \dots \begin{bmatrix} \cos(S_2 - \pi) & -\sin(S_2 - \pi) \\ \sin(S_2 - \pi) & \cos(S_2 - \pi) \end{bmatrix} \begin{bmatrix} \cos(S_1 - \pi) & -\sin(S_1 - \pi) \\ \sin(S_1 - \pi) & \cos(S_1 - \pi) \end{bmatrix} \begin{bmatrix} \cos(2\pi) \\ \sin(2\pi) \end{bmatrix} \\
&= \dots \begin{bmatrix} -\cos S_2 & \sin S_2 \\ -\sin S_2 & -\cos S_2 \end{bmatrix} \begin{bmatrix} -\cos S_1 & \sin S_1 \\ -\sin S_1 & -\cos S_1 \end{bmatrix} \begin{bmatrix} 1 \\ 0 \end{bmatrix}. \tag{21}
\end{aligned}$$

This suggests using a loop in a computer subroutine.

Due to the projection, $|\omega_f|$ never exceeds the area of one hemisphere (2π steradians). Thus, there is no ambiguity due to multiple revolutions. The half-angle formula $\tan x/2 = (1 - \cos x)/\sin x$ suggests

$$|\omega_f| = 2 \arctan \frac{1 - \cos|\omega_f|}{\sin|\omega_f|}. \tag{22}$$

There are three reasons to use the half-angle formula instead of the usual $\tan x = \sin x/\cos x$. One is that a computer's atan2 function ranges over $(-\pi, +\pi)$ instead of $[0, 2\pi)$ which we desire. In the half-angle formula, the numerator is never negative and the denominator is signed; atan2 ranges over $[0, \pi)$ and $|\omega_f|$ ranges over $[0, 2\pi)$ as desired.

Another reason is that the ultimate goal is to calculate the signed ω_f , which ranges over $(-2\pi, +2\pi)$. We produce the correctly signed ω_f by multiplying Equation (22) by $\text{sign}(\Delta z)$:

$$\omega_f = \text{sign}(\Delta z) \cdot 2 \arctan \frac{1 - \cos|\omega_f|}{\sin|\omega_f|} = 2 \arctan \frac{\text{sign}(\Delta z) \cdot (1 - \cos|\omega_f|)}{\sin|\omega_f|}. \tag{23}$$

The final reason is that a nice cancellation occurs when we calculate a triangle's ω_f .

2.5.4. Area of a Spherical Triangle

Marked simplifications occur when the polygon is a triangle. One occurs because the numerators of all three $\sin S_j$ expressions (Equation 20), $|\hat{\mathbf{r}}_i \bullet \hat{\mathbf{r}}_j \times \hat{\mathbf{r}}_k|$, are equal. Another simplification occurs when we expand the iterative computation of $\cos|\omega_f|$ and $\sin|\omega_f|$ for the three vertices P_1, P_2, P_3 of a triangle. Routine, tedious algebra yields

$$\cos|\omega_f| = 1 - \frac{|\hat{\mathbf{r}}_1 \bullet \hat{\mathbf{r}}_2 \times \hat{\mathbf{r}}_3|^2}{(1 + c_{12})(1 + c_{23})(1 + c_{31})} \quad (24)$$

$$\sin|\omega_f| = \frac{1 + c_{12} + c_{23} + c_{31}}{(1 + c_{12})(1 + c_{23})(1 + c_{31})} \cdot |\hat{\mathbf{r}}_1 \bullet \hat{\mathbf{r}}_2 \times \hat{\mathbf{r}}_3|. \quad (25)$$

We absorb an upcoming sign (Δz) factor in the following way. For a convex polygon such as our triangle, we can calculate the face normal vector as the cross product of along-the-edge vectors. An unnormalized vector aligned with a convex polygon's face normal is

$$\mathbf{n}_f = (\mathbf{r}_2 - \mathbf{r}_1) \times (\mathbf{r}_3 - \mathbf{r}_2) = \mathbf{r}_1 \times \mathbf{r}_2 + \mathbf{r}_2 \times \mathbf{r}_3 + \mathbf{r}_3 \times \mathbf{r}_1.$$

From the definition $\Delta z = \mathbf{r}_f \bullet \hat{\mathbf{n}}_f$, substitute $\mathbf{r}_f \rightarrow \mathbf{r}_1$ and calculate $\text{sign}(\Delta z)$ as

$$\begin{aligned} \text{sign}(\Delta z) &= \text{sign}(\mathbf{r}_f \bullet \hat{\mathbf{n}}_f) = \text{sign}(\mathbf{r}_1 \bullet \mathbf{n}_f) = \text{sign}(\mathbf{r}_1 \bullet (\mathbf{r}_1 \times \mathbf{r}_2 + \mathbf{r}_2 \times \mathbf{r}_3 + \mathbf{r}_3 \times \mathbf{r}_1)) \\ &= \text{sign}(\mathbf{r}_1 \bullet \mathbf{r}_2 \times \mathbf{r}_3) = \text{sign}(\hat{\mathbf{r}}_1 \bullet \hat{\mathbf{r}}_2 \times \hat{\mathbf{r}}_3). \end{aligned}$$

Then

$$\text{sign}(\Delta z) |\hat{\mathbf{r}}_1 \bullet \hat{\mathbf{r}}_2 \times \hat{\mathbf{r}}_3| = \hat{\mathbf{r}}_1 \bullet \hat{\mathbf{r}}_2 \times \hat{\mathbf{r}}_3. \quad (26)$$

When we incorporate Equations (24)–(26) into Equation (23), we get the following simple expression for a triangle's signed ω_f :

$$\begin{aligned} \iint_{\text{triangle}} \frac{\Delta z}{r^3} dS &= \omega_f = 2 \arctan \frac{\text{sign}(\Delta z)(1 - \cos|\omega_f|)}{\sin|\omega_f|} \\ &= 2 \arctan \frac{\text{sign}(\Delta z) \left[1 - \left(1 - \frac{|\hat{\mathbf{r}}_1 \bullet \hat{\mathbf{r}}_2 \times \hat{\mathbf{r}}_3|^2}{(1 + c_{12})(1 + c_{23})(1 + c_{31})} \right) \right]}{\frac{1 + c_{12} + c_{23} + c_{31}}{(1 + c_{12})(1 + c_{23})(1 + c_{31})} |\hat{\mathbf{r}}_1 \bullet \hat{\mathbf{r}}_2 \times \hat{\mathbf{r}}_3|} \\ &= 2 \arctan \frac{\text{sign}(\Delta z) |\hat{\mathbf{r}}_1 \bullet \hat{\mathbf{r}}_2 \times \hat{\mathbf{r}}_3|}{1 + c_{12} + c_{23} + c_{31}} \end{aligned}$$

$$\begin{aligned}
 &= 2 \arctan \frac{\hat{\mathbf{r}}_1 \bullet \hat{\mathbf{r}}_2 \times \hat{\mathbf{r}}_3}{1 + \hat{\mathbf{r}}_1 \bullet \hat{\mathbf{r}}_2 + \hat{\mathbf{r}}_2 \bullet \hat{\mathbf{r}}_3 + \hat{\mathbf{r}}_3 \bullet \hat{\mathbf{r}}_1} \\
 &= 2 \arctan \frac{\mathbf{r}_1 \bullet \mathbf{r}_2 \times \mathbf{r}_3}{r_1 r_2 r_3 + r_1 (\mathbf{r}_2 \bullet \mathbf{r}_3) + r_2 (\mathbf{r}_3 \bullet \mathbf{r}_1) + r_3 (\mathbf{r}_1 \bullet \mathbf{r}_2)}. \quad (27)
 \end{aligned}$$

The factors $|\hat{\mathbf{r}}_1 \bullet \hat{\mathbf{r}}_2 \times \hat{\mathbf{r}}_3|, (1 + c_{12}), (1 + c_{23}), (1 + c_{31})$ are never negative and canceling them does not affect the quadrant returned by \arctan .

Both the numerator and denominator in Equation (27) are signed. They can be presented as separate arguments to a computer's atan2 function to calculate a triangle's $\omega_f = \iint (\Delta z / r^3) dS$ in the range $(-\pi, +\pi)$.

2.6. SUMMARY: POLYHEDRON GRAVITATION

Symbols G and σ represent the gravitational constant and the polyhedron's constant density. Suffices e and f indicate edge and face, respectively.

Each polyhedron face has an outward-pointing face normal vector $\hat{\mathbf{n}}_f$ and face dyad $\mathbf{F}_f = \hat{\mathbf{n}}_f \hat{\mathbf{n}}_f$. Each edge of each face has an outward-pointing edge normal vector $\hat{\mathbf{n}}_e^f$ perpendicular to both $\hat{\mathbf{n}}_f$ and the edge. For the edge connecting vertices 1 and 2 shared by faces A and B , the edge dyad is $\mathbf{E}_{12} = \hat{\mathbf{n}}_A \hat{\mathbf{n}}_{12}^A + \hat{\mathbf{n}}_B \hat{\mathbf{n}}_{21}^B$, with other \mathbf{E}_{es} defined similarly.

Let \mathbf{r}_i represent the vector from the variable field-point location to polyhedron vertex P_i , and let $r_i = \|\mathbf{r}_i\|$ be its length. For the polyhedron edge connecting vertices P_i and P_j of constant length e_{ij} , the dimensionless per-edge factor L_e is

$$L_e \equiv \int_e \frac{1}{r} ds = \int_{P_i}^{P_j} \frac{1}{r} ds = \ln \frac{r_i + r_j + e_{ij}}{r_i + r_j - e_{ij}}. \quad (7)$$

For a triangular face f bounded by vertices P_i, P_j, P_k , the dimensionless per-face factor ω_f is

$$\omega_f = \iint_{\text{triangle}} \frac{\Delta z}{r^3} dS = 2 \arctan \frac{\mathbf{r}_i \bullet \mathbf{r}_j \times \mathbf{r}_k}{r_i r_j r_k + r_i (\mathbf{r}_j \bullet \mathbf{r}_k) + r_j (\mathbf{r}_k \bullet \mathbf{r}_i) + r_k (\mathbf{r}_i \bullet \mathbf{r}_j)}. \quad (27)$$

Using these definitions, the gravitational potential, attraction, gravity gradient matrix, and Laplacian of a constant density polyhedron are expressed intrinsically, in closed form, thus:

$$U = \frac{1}{2} G \sigma \sum_{e \in \text{edges}} \mathbf{r}_e \bullet \mathbf{E}_e \bullet \mathbf{r}_e \cdot L_e - \frac{1}{2} G \sigma \sum_{f \in \text{faces}} \mathbf{r}_f \bullet \mathbf{F}_f \bullet \mathbf{r}_f \cdot \omega_f \quad (10)$$

$$\nabla U = -G \sigma \sum_{e \in \text{edges}} \mathbf{E}_e \bullet \mathbf{r}_e \cdot L_e + G \sigma \sum_{f \in \text{faces}} \mathbf{F}_f \bullet \mathbf{r}_f \cdot \omega_f \quad (15)$$

$$\nabla \nabla U = G \sigma \sum_{e \in \text{edges}} \mathbf{E}_e \cdot L_e - G \sigma \sum_{f \in \text{faces}} \mathbf{F}_f \cdot \omega_f \quad (16)$$

$$\nabla^2 U = -G\sigma \sum_{f \in \text{faces}} \omega_f. \quad (17)$$

There is a straightforward progression from potential to attraction to gravity gradient matrix.

3. Modeling Asteroid Gravity Fields

A prime application of the polyhedron approach is for modeling asteroid gravity fields. Asteroid shapes have been estimated from optical information obtained during a spacecraft flyby (Simonelli *et al.*, 1993; Thomas *et al.*, 1994; Thomas *et al.*, 1995) and from range-Doppler radar imaging of near-Earth asteroids from ground-based stations (Hudson *et al.*, 1994).

In this section we use a shape model of asteroid 4769 Castalia to compare harmonic, mascon, and polyhedral approaches to asteroid gravitation. The shape data were obtained from range-Doppler imaging of Castalia from the Arecibo radio antenna during a close approach to Earth (Hudson *et al.*, 1994). The model consists of 3300 faces, yielding a shape resolution on the order of 5° as measured at the equator. Figure 11 shows a computer model and a contour map of Castalia's shape. The minimum radius is approximately 0.3 km at the poles of the asteroid, the maximum radius is approximately 0.8 km at the ends, and the mean radius is 0.543 km. The density is assumed to be 2.1 g/cm^3 , giving a total mass of $1.4 \times 10^{12} \text{ kg}$ (Scheeres *et al.*, 1995). See Figure 12 for contour plots of the magnitude of the force attraction based on this model.

Figures 13, 14, 16 and 17 show contour maps of the percent error of the harmonic and mascon fields relative to the polyhedron field. For comparison of the potential, the polyhedron potential is subtracted from the harmonic or mascon potential and the difference is divided by the polyhedron potential. For comparison of the attraction, the magnitude of the vector difference of the polyhedron attraction from the harmonic or mascon attraction is divided by the polyhedron attraction magnitude.

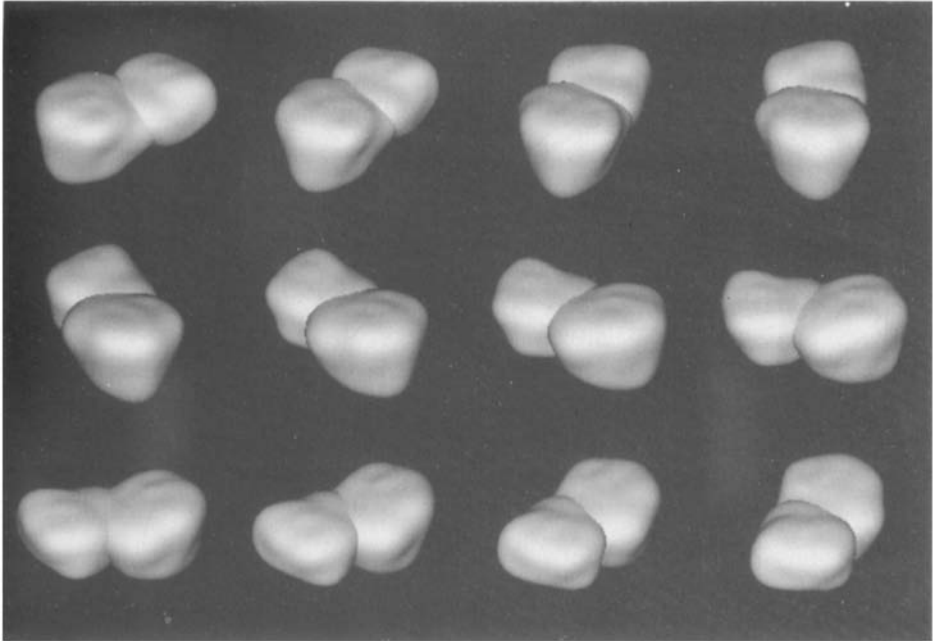
Neither the harmonic nor mascon model yields any information about whether the field point is inside or outside the body.

3.1. HARMONIC FIELD

The coefficients of a degree and order 20 exterior harmonic expansion were calculated by performing surface integrals over the asteroid shape, using the existing polyhedron to tessellate the asteroid shape. In performing the integrations, the exact surface area projection for each elemental area (as calculated in this paper) was used with the integrand being evaluated at the center of each elemental area.

For a harmonic expansion, the radius of the reference sphere may be conveniently equated with the maximum radial dimension of the body (the circumscribing

(A)



(B)

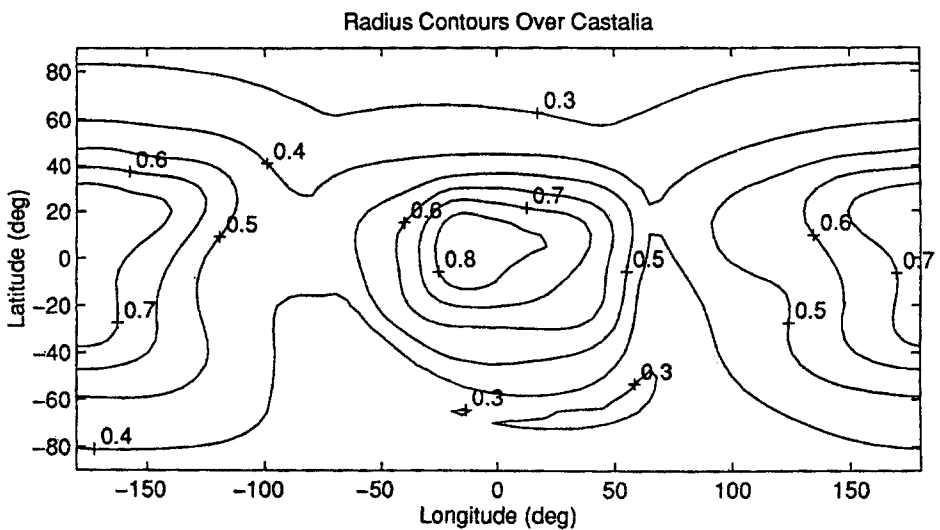


Figure 11. (a) A representation of asteroid 4769 Castalia's radar resolved shape model and (b) a contour map of its surface radius (photo courtesy of JPL/CALTECH).

sphere). When evaluating the harmonic expansion inside of this sphere the exterior series may diverge (and in general will for a generic body) (Heiskanen *et al.*, 1967, p. 60).

Figure 13 shows contour plots of the percent of potential error due to the harmonic model's truncation and divergence, relative to the polyhedral model.

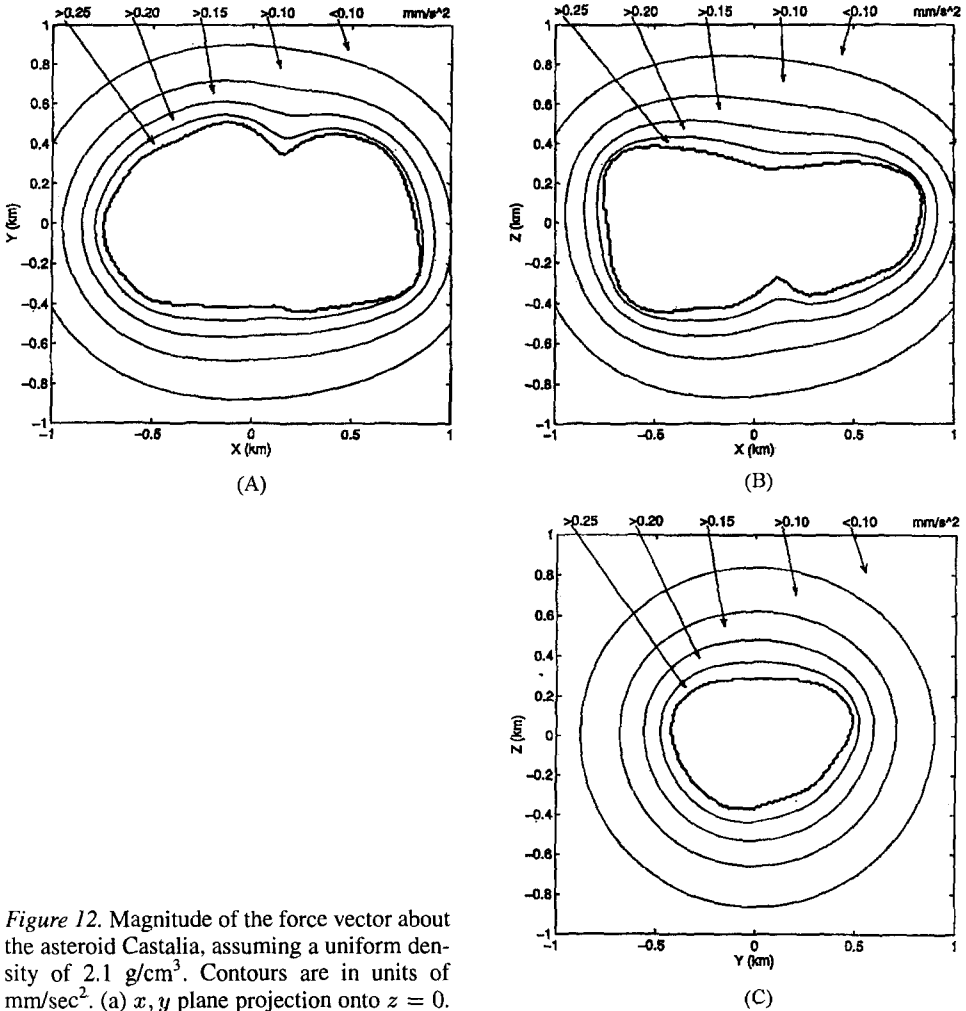


Figure 12. Magnitude of the force vector about the asteroid Castalia, assuming a uniform density of 2.1 g/cm^3 . Contours are in units of mm/sec^2 . (a) x, y plane projection onto $z = 0$. (b) x, z plane projection onto $y = 0$. (c) y, z plane projection onto $x = 0$.

Figure 13a, b, and c are in the $z = 0$, $y = 0$, and $x = 0$ planes, respectively. The outermost contour is 0.1% error and circumscribes contours of 1%, 10%, and 100% error. The innermost outline is Castalia's surface.

Figure 14 shows contour plots of the harmonic model's attraction magnitude errors, again in the $z = 0$, $y = 0$ and $x = 0$ planes. The harmonic expansion diverges inside its circumscribing sphere and errors increase quickly. Outside, the harmonic expansion converges rapidly upon the correct result.

These figures nicely show the divergence of the harmonic expansions, and the waviness in the contours which arises from truncating the harmonic series.

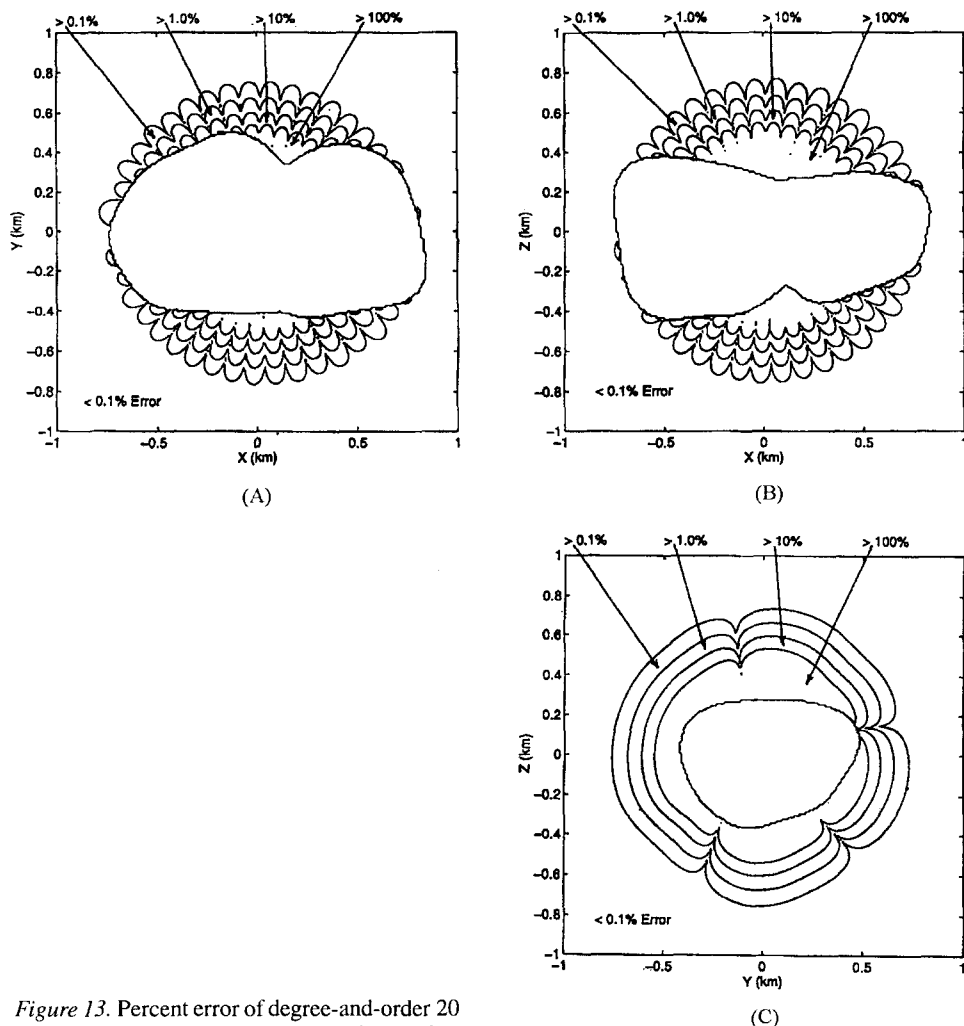


Figure 13. Percent error of degree-and-order 20 harmonic potential with respect to the polyhedral potential. (a,b,c, as in Fig. 12).

3.2. MASCON FIELD

A simple approximation for an arbitrarily shaped body is to fill the shape with a uniformly spaced grid of point masses. This mascon approximation does not suffer series divergence or truncation as does the harmonic approach. However, when considering the geometry of this approximation, it is clear that the solid body is being replaced with a topologically different body composed of spherical balls. Assuming that the spheres touch without overlap, the ratio of the volume of a radius r sphere to a cube of edge length $2r$ is ~ 0.52 . The mascon model replaces the true body's continuous mass distribution with a field derived of spheres with

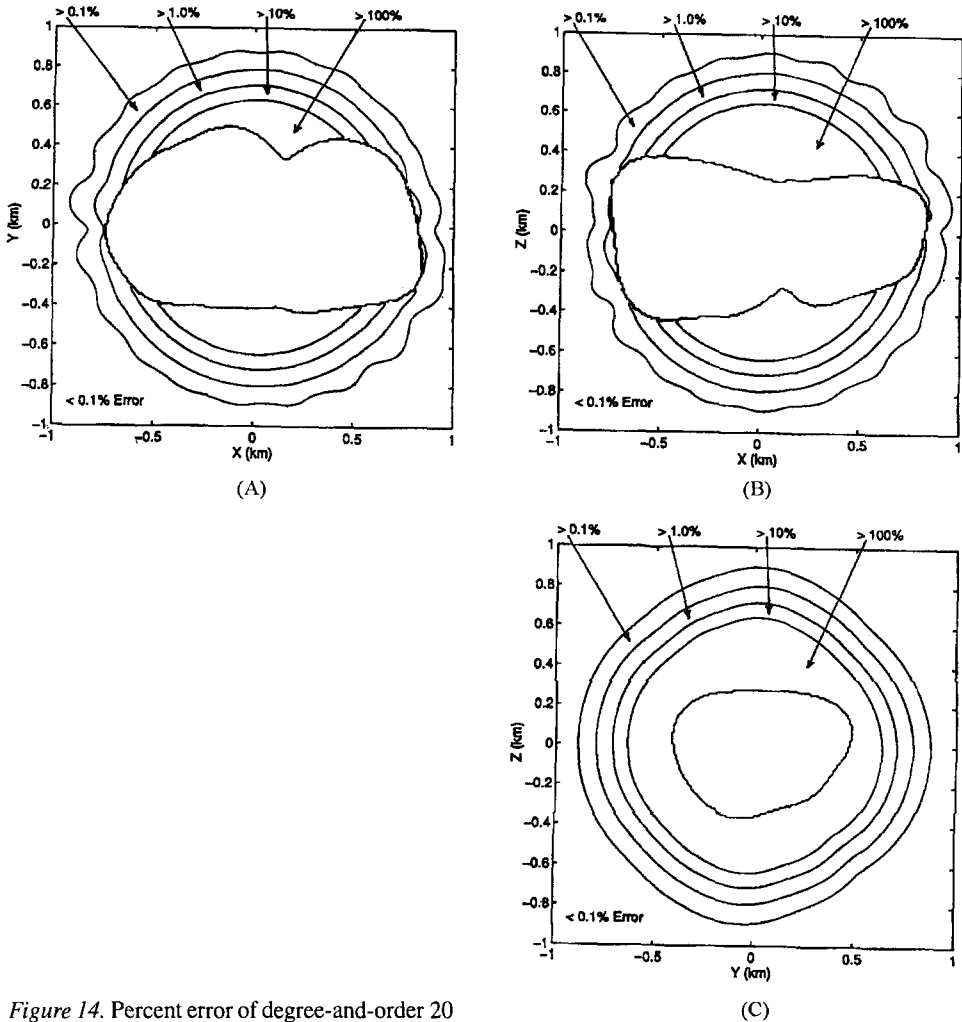


Figure 14. Percent error of degree-and-order 20 harmonic attraction with respect to the polyhedral attraction. (a,b,c, as in Fig. 12).

density approximately twice the nominal density and with $\sim 48\%$ of the body being vacant.

To clearly demonstrate the error involved with an individual mascon, Figure 15 shows the percent error between the attraction of a unit cube and a unit sphere having equal masses. The largest error on the surface of the cube approaches 50% at the midpoint of each face of the cube. The error is not uniformly less than 0.1% until further than 2.5 radii from the cube center.

Simple estimates show that the modeling error is proportional to the size of each individual mascon (i.e. to the resolution), while the number of mascons needed is inversely proportional to the cube of the size of each mascon. Thus, to drive the

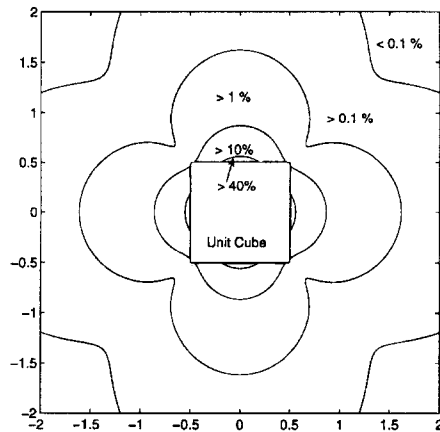


Figure 15. Percent attraction error of a unit sphere as compared with a unit cube of the same mass. This is the generic picture of the error associated with the mascon approximation. The maximum error approaches 50% on the sides and does not diminish to 0.1% until greater than 2.5 units from the center.

error of the mascon model down by an order of magnitude will, in general, require a 3 order of magnitude increase in the number of individual mascon particles. Thus, accurate representations of the gravity field near the surface of an irregularly shaped body may require large numbers of individual mascons.

For this comparison, Castalia was filled with approximately 3300 point masses corresponding to a modeling resolution of 59 meters, all appropriately scaled to yield the same total mass. The potential field of this mascon model compares well with the true potential, with agreement to within 0.1% over most of the body, even when evaluated close to the surface. Since the agreement is so good, we do not exhibit any figure of mascon potential errors.

Figure 16 shows contour plots of the percent errors in mascon attraction magnitude. The attraction errors are between 1 and 10% over most of the surface but swell to over 10% at isolated pockets, depending on the model resolution. However, away from the asteroid the mascon attraction error does not diminish as quickly as does the harmonic expansion. Instead, mascon error remains between 0.1 and 1% over most of the space away from the body shown in the plots. Increasing the resolution by a factor of 1.4 (to 41 meters) increases the total number of mascon particles to ~ 9700 , yet still has appreciable errors (Figure 17).

The force magnitudes found using mascons are less accurate than those found with the harmonic expansions in its convergence region. The process of differentiation tends to accelerate convergence and divergence of the harmonic expansion, thus delineating the radius of convergence more clearly. For the mascon model, the process of differentiation exposes the presence of the point masses and extends the error due to their existence well away from the body. Finally, when evaluated over the surface of the body, appreciable errors (greater than 10%) in the mascon

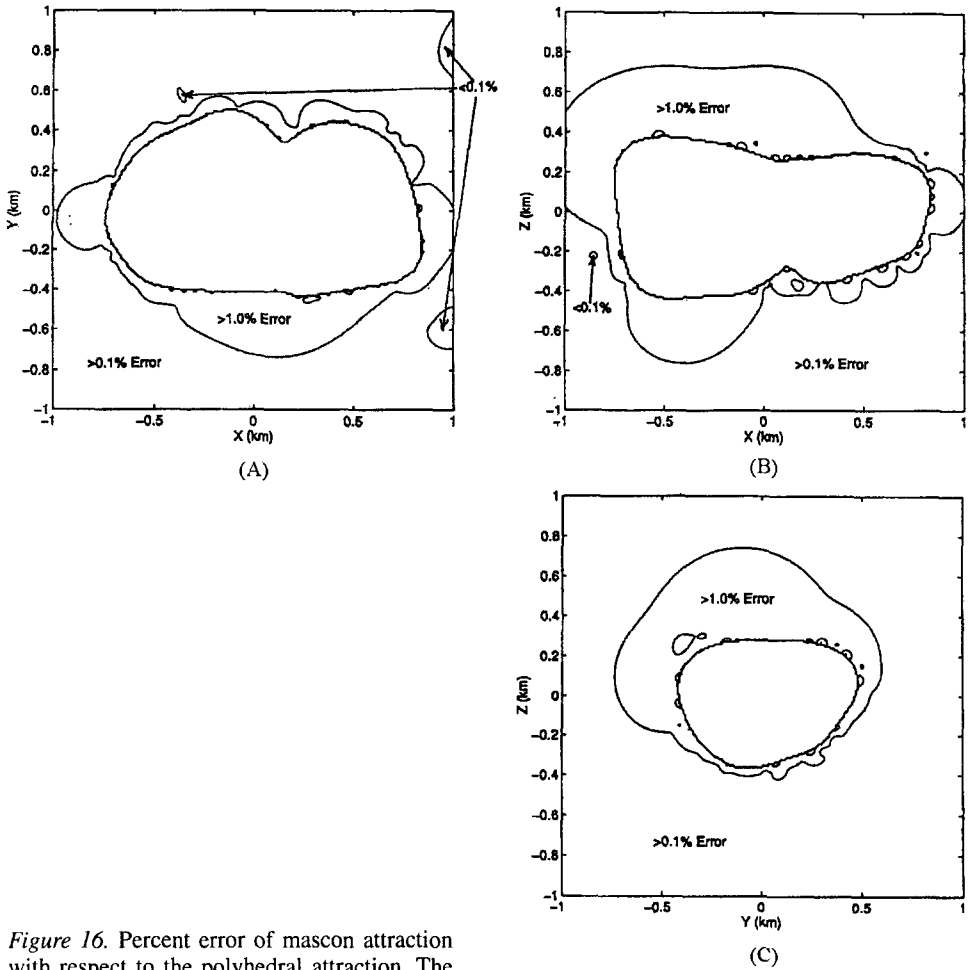


Figure 16. Percent error of mascon attraction with respect to the polyhedral attraction. The contour circles at the asteroid surface correspond to regions of error $>10\%$. The model includes 3300 mascons on a 59 meter grid. (a,b,c, as in Fig. 12).

attraction exist at isolated locations. The size of these regions depends directly on the resolution used for the mascon model.

3.3. MODELING DENSITY VARIATIONS

Another application of polyhedral gravitation is to simulate density variations within an asteroid. Such a possibility will be forthcoming when the Near Earth Asteroid Rendezvous (NEAR) spacecraft rendezvous with the asteroid 433 Eros in early 1999 (Miller *et al.*, 1995). During the course of the mission, a harmonic representation of the asteroid gravity field will be estimable to ~ 10 th degree

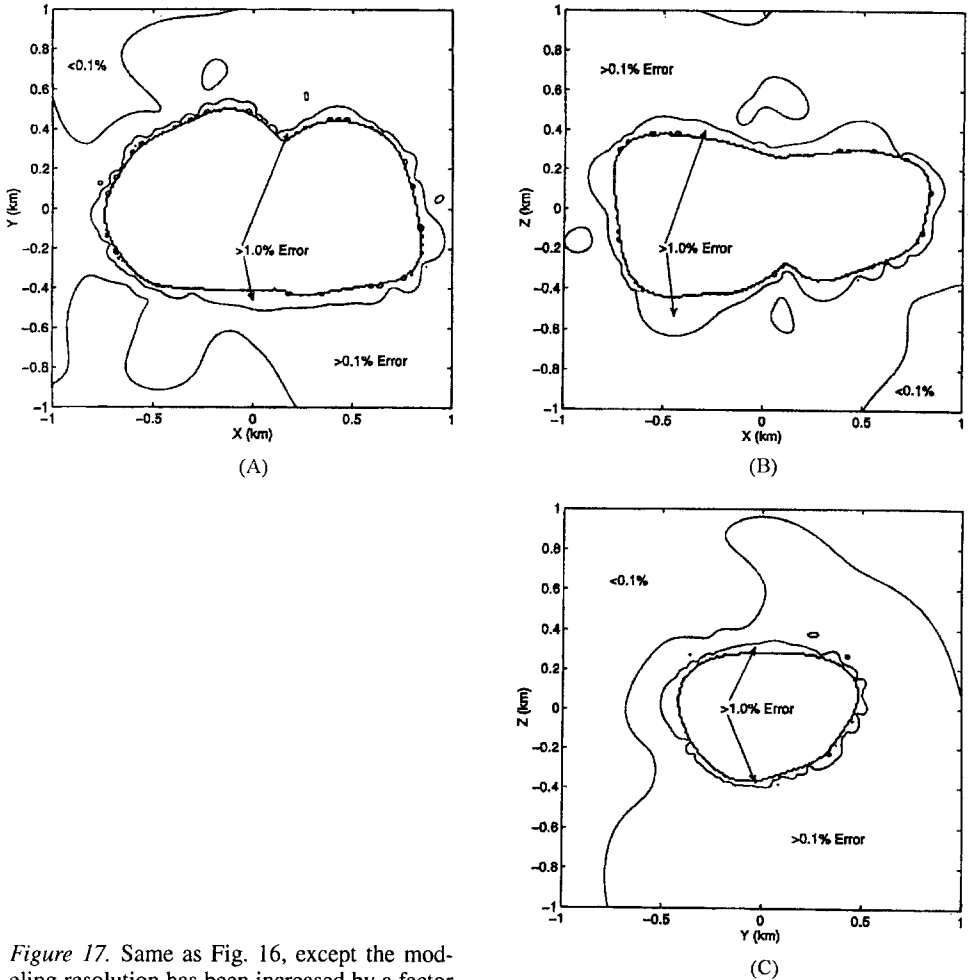


Figure 17. Same as Fig. 16, except the modeling resolution has been increased by a factor of 1.4 and the number of mascons has been increased by a factor of 3. The contour circles at the asteroid surface correspond to regions of error $> 10\%$. (a,b,c as in Fig. 12).

and order. Any density variations expressed by the harmonic expansion might be simulated by adding and subtracting small polyhedra internal to an overall polyhedral model.

Given the main shape of the asteroid, it will be necessary to compute the resulting gravity field over the appropriate grid only once. Then candidate shapes for the internal topology of the asteroid can be computed and added to the existing field. A necessary constraint is that the total mass of the asteroid (which will be well known) be held constant. This is possible since the volumes of the asteroid

and interior shapes can be directly computed from the polyhedral shape, and the necessary densities chosen so that the sum

$$M = \rho_0 V_0 + \sum_{i=1}^N (\rho_i - \rho_0) V_i$$

is constant, where M is the total mass of the asteroid, V_0 the volume of the total asteroid shape, ρ_0 the assumed nominal density of the asteroid, V_i the volume of the i th internal addition and ρ_i the density of the i th internal addition. It is possible, if desired, to fix the nominal density ρ_0 equal to M/V_0 , although then the additional volumes and densities must be chosen so that they sum to zero. In practice it will be simpler to specify the candidate internal volumes and densities and then choose ρ_0 such that

$$\rho_0 = \left(M - \sum_{i=1}^N \rho_i V_i \right) / \left(V_0 - \sum_{i=1}^N V_i \right).$$

4. Conclusions

We have presented a new derivation of a constant-density polyhedron's gravitational potential, attraction, gravity gradient matrix, and Laplacian of potential. The derivation is analytic throughout; there are no numerical quadratures. Results are expressed intrinsically in closed form and involve only elementary functions (arctangent and logarithm). There is a straightforward progression from potential to attraction to gravity gradient.

The polyhedral approach provides a simple means of determining whether a point is inside or outside of a polyhedron, since the potential satisfies Laplace's equation outside the body and Poisson's equation inside. The Laplacian can be calculated at essentially no additional cost if the potential or attraction is also being calculated, such as in a spacecraft simulation.

Our work can be used for studies of regolith motion, ejecta trajectories, and orbit stability in the vicinity of irregular-shaped bodies, where other approaches suffer accuracy and convergence problems. Errors exceeding 100% have been demonstrated with the classic harmonic approach. Mascon attraction errors decrease slowly as the distance from the asteroid surface increases.

There might be utility in superimposing polyhedron and conventional spherical-harmonic expressions in a planetary gravitation field, to include details such as ocean trenches, mountain ranges, or density variations.

A drawback to the polyhedral approach is the greater compute time needed, as the entire surface must be summed over to achieve one force value. With the current computer workstations available, it is not prohibitive to make such calculations,

and even numerical trajectory integrations are possible using asteroid shapes with a few thousand faces.

New investigations into using parallel computing techniques should yield a significant speed-up in computation time. The polyhedron expressions can be evaluated in three phases once a field point has been chosen: (1) Calculate vectors and distances from the field point to all of the polyhedron's vertices. Results serve as \mathbf{r}_e and \mathbf{r}_f in subsequent phases; (2) Calculate and accumulate edge terms involving L_e and \mathbf{E}_e ; and (3) Calculate and accumulate face terms involving ω_f and \mathbf{F}_f . Individual tasks in each phase can be calculated in parallel, and phases (2) and (3) can be calculated in parallel.

Acknowledgements

Comments from two anonymous reviewers helped us improve the presentation, and prevented us from making an incorrect statement. Early portions of this work were supported by NASA Graduate Student Researchers Program fellowship NGT 50573.

References

- Bannerjee, B. and Gupta, S.P.D.: 1977, *Geophysics* **42**, 1053.
 Barnett, C.T.: 1976, *Geophysics* **41**(6), 1353.
 Broucke, R.A.: 1995, 'Closed Form Expressions for Some Gravitational Potentials: Triangle, Rectangle, Pyramid and Polyhedron', AAS/AIAA Spaceflight Mechanics Meeting, Albuquerque, New Mexico, February 13–16, paper AAS 95–190.
 Cady, J.W.: 1980, *Geophysics* **45**(10), 1507.
 Geissler, P., Petit, J.-M., Durda, D., Greenberg, R., Bottke, W., Nolan, M. and Moore, J.: 1996, *Icarus* **120**, 140.
 Goldstein, H.: 1980, *Classical Mechanics* (second edition), Reading, Mass: Addison-Wesley.
 Golizdra, G.Ya.: 1981, *Izvestiya, Physics of the Solid Earth* **17**(8), 625.
 Goździewski, K. and Maciejewski, A.J.: 1981, 'On the Gravitational Fields of Pandora and Prometheus' (preprint).
 Grafarend, E. and Engles, J.: 1994, *Manuscripta Geodaetica* **19**, 18.
 Greenwood, M.D.: 1978, *Foundations of Applied Mathematics*, Englewood Cliffs, N.J.: Prentice-Hall.
 Greenwood, D.T.: 1988, *Principles of Dynamics* (second edition), Englewood Cliffs, N.J.: Prentice-Hall.
 Heiskanen, W.A. and Moritz, H.: 1967, *Physical Geodesy*, San Francisco: W.H. Freeman and Co.
 Hoppe, H., DeRose, T., Duchamp, T., McDonald, J. and Stuetzle, W.: 1992, 'Surface Reconstruction from Unorganized Points', Proceedings of SIGGRAPH '92 (Chicago, Illinois, July 26–31, 1992), in: *Computer Graphics* **26**(2), 71–78 New York: ACM SIGGRAPH.
 Hudson, R.S. and Ostro, S.J.: 1994, *Science* **263**, 940.
 Kaula, W.M.: 1966, *Theory of Satellite Geodesy*, Waltham, Mass.: Blaisdell.
 Kwok, Y.-K.: 1991, *Geophysical Prospecting (Netherlands)* **39**(3), 435.
 MacMillan, W.D.: 1930, *The Theory of the Potential*, New York: McGraw-Hill. Republished by Dover, New York (1958).
 MacMillan, W.D.: 1936, *Dynamics of Rigid Bodies*, New York: McGraw-Hill.
 Malovichko, A.I.K.: 1963, 'Hundred-year anniversary of the work of F.A. Sludskiy on the attraction of homogeneous polyhedra', *Questions in the Processing and Interpretation of Geophysical Observations. Perm**, No. 4.

- Miller, J.K., Williams, B.G., Bollmann, W.E., Davis, R.P., Helfrich, C.E., Scheeres, D.J., Synnott, S.P., Wang, T.C. and Yeomans, D.K.: 1995, *Journal of the Astronautical Sciences* **43**(4), 453.
- Montana, C.J., Mickus, K.L. and Peebles, W.J.: 1992, *Computers and Geosciences (UK)* **18**(5), 587.
- Moritz, H.: 1980, *Advanced Physical Geodesy*, Abacus Press.
- Nagy, D.: 1966, *Geophysics* **31**(2), 362.
- Okabe, M.: 1979, *Geophysics* **44**(4), 730–741.
- Plouff, D.: 1976, *Geophysics* **41**, 727–741.
- Pohánka, V.: 1988, *Geophysical Prospecting* **36**, 733.
- Scheeres, D.J., Ostro, S.J., Hudson, R.S. and Werner, R.A.: 1996, *Icarus* **121**, 67.
- Selby, S.M. (ed.): 1965, *CRC Standard Mathematical Tables*, Cleveland, Ohio: The Chemical Rubber Co.
- Simonelli, D.P., Thomas, P.C., Carcich, B.T. and Veverka, J.: 1993, *Icarus* **103**, 49.
- Strakhov, V.N. and Lapina, M.I.: 1990, *Geophysical Journal (UK)* **8**(6), 740.
- Telford, W.M., Geldart, L.P., Sheriff, R.E. and Keys, D.A.: 1976, *Applied Geophysics*, New York: Cambridge University Press.
- Thomas, P., Veverka, J. and Dermott, S.: 1986, '17 Small Satellites', in *Satellites*, J.A. Burns and M.S. Matthews (eds.), Tucson: University of Arizona Press, pp. 802–835.
- Thomas, P.C.: 1993, *Icarus* **105**, 326.
- Thomas, P.C., Veverka, J., Simonelli, D., Helfenstein, P., Carcich, B., Belton, M.J.S., Davies, M.E. and Chapman, C.: 1994, *Icarus* **107**, 23.
- Thomas, P.C., Belton, M.J.S., Carcich, B., Chapman, C., Davies, M.E., Sullivan, R. and Veverka, J.: 1995, 'The Shape of Ida' (preprint).
- Waldvogel, J.: 1976, *Journal of Applied Mathematics and Physics (ZAMP)* **27**, 867.
- Waldvogel, J.: 1979, *Journal of Applied Mathematics and Physics (ZAMP)* **30**, 388.
- Werner, R.A.: 1994, *Celestial Mechanics and Dynamical Astronomy* **59**, 253.